A two-phase, pore-scale reactive transport model for the kinetic interface- sensitive tracer

Enter authors here: H. Gao[1], A. B. Tatomir[2,1], and N. K. Karadimitriou[3], and H. Steeb[3,4], and M. Sauter[1]

[1]Department of Applied Geology, University of Göttingen, 37073, Göttingen, Germany.

[2]Department of Earth Sciences, Uppsala University, 752 36 Uppsala, Sweden.

[3]Institute of Applied Mechanics (CE), University of Stuttgart, 70569 Stuttgart, Germany.

[4]Stuttgart Center for Simulation Technology, Pfaffenwaldring 5a, 70569 Stuttgart, Germany

Corresponding author: Alexandru Tatomir (alexandru.tatomir@geo.uu.se)

Key Points:

- We develop a pore-scale two-phase flow reactive transport model for KIS tracer based on phase-field method.
- We provide a model verification and validation, then we demonstrate it in NAPL/water drainage scenarios in a conceptual porous domain.
- This study demonstrates that KIS tracers measure the mobile fluid-fluid interfacial area.

Abstract:

Previous laboratory experiments with KIS tracers have shown promising results with respect to the quantification of fluid-fluid interfacial area (IFA) for dynamic, two-phase flow conditions. However, pore-scale effects relevant for two-phase flow (e.g. the formation of hydrodynamically stagnant/ immobile zones) are not yet fully understood, and quantitative information in how far these effects influence the transport of the tracer reaction products is not yet available. Therefore, a pore-scale numerical model that includes two-phase, reactive flow and transport of the KIS tracer at the fluid-fluid interface is developed. We propose a new method to quantitatively analyze how the concentration of the KIS-tracer reaction product in the effluent is affected by the presence of immobile zones. The model employs the phase field method (PFM) and a new continuous mass transfer formulation, consistent with the PFM. We verify the model with the analytical solution of a reaction-diffusion process for two-phase flow conditions in a conceptual capillary tube. The applicability of the model is demonstrated in NAPL/water drainage scenarios in a conceptual porous domain, comparing the results in terms of the spatial distribution of the phases and the quantified macro-scale parameters (saturation, capillary pressure, IFA and solute concentration). Furthermore, we distinguish the mobile and immobile zones based on the local Péclet number, and the corresponding solute mass in these two zones is quantified. Finally, we show that the outflow concentration can be employed to selectively determine the mobile part of the IFA.

1. Introduction

Understanding multi-phase, multi-component, reactive flow and transport in porous media is important for a wide range of scientific and engineering applications. Such applications comprise for example the geological storage of carbon dioxide, groundwater remediation, enhanced oil recovery, material manufacturing, etc. (Miller et al. 1990; Hassanizadeh and Gray 1990; Reeves and Celia 1996). In this context, the quantification of the magnitude of the Fluid-Fluid Interfacial Area (FIFA) is essential for studying reactive multi-phase flow and transport in porous materials (Miller et al. 1990). For example, in geological storage of CO_2, both the rate of CO_2 dissolution in brine and the extent of the residual trapping are determined by the FIFA (Tatomir et al. 2018). Existing techniques for FIFA measurement mainly comprise tracer techniques, e.g., Interfacial Partitioning Tracer Tests (IPTT) (Brusseau et al. 2009, 2010; McDonald et al. 2016), imaging techniques e.g. X-Ray Computed Micro-Tomography (XMT) (Dalla et al. 2002; Culligan et al. 2004; Porter et al. 2010; Wildenschild and Sheppard 2013; McDonald et al. 2016) and Photo-luminescent Volumetric Imaging (PVI) (Montemagno and Gray 1995). However, one limitation of these methods is that they are mainly applied under steady state or quasi-static conditions (Tatomir et al. 2018). The Kinetic Interface Sensitive (KIS) tracer method was developed for tracking the FIFA in dynamic processes (Tatomir et al. 2016b; Tatomir et al. 2018), as an alternative to IPTT and XMT methods for determining the FIFA under transient conditions (Tatomir et al. 2018; Tatomir et al. 2020).

1.1Kinetic Interfacial Sensitive tracer: theoretical background

The KIS tracer concept and application is described in detail in Schaffer et al. (2013) and Tatomir et al. (2018). A chemically stable KIS tracer compound was identified to

be the phenyl naphthalene-2-sulfonate (2-NSAPh) by Schaffer et al. (2013). The 2-NSAPh is a non-polar hydrolysable phenolic ester which dissolves in nonpolar liquids, such as supercritical CO_2, or its analogue liquid-phase n-octane (see Schaffer et al. (2013)). Thus, a KIS tracer is dissolved in a nonpolar liquid usually acting as a non-wetting phase. With the KIS tracer dissolved, the nonpolar liquid is injected into the initially water saturated porous medium and the KIS tracers are adsorbed onto the fluid-fluid interface (**Figure 1**). The adsorption process is assumed to follow Langmuir's isotherm (Eq.(1)):

$$\frac{c_i}{c_{i,max}} = \frac{K_L \cdot c_a}{1 + K_L \cdot c_a} \tag{1}$$

where K_L is the Langmuir adsorption coefficient of the (non-wetting phase) dissolved KIS tracer at the fluid-fluid interface, c_a the concentration of the KIS tracer in the (bulk) non-wetting phase, c_i the KIS concentration at the interface, usually assumed to be approximately equal to the maximum concentration of the saturated interface $c_{i,max}$. The adsorbed 2-NSAPh molecules at the fluid-fluid interface when getting in contact with the water molecules undergo an irreversible hydrolysis reaction.

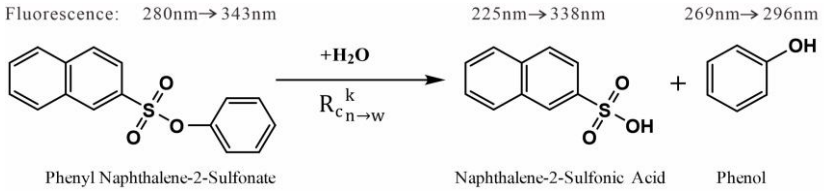

(2)

Due to the excess supply of the tracer in the non-wetting phase (high c_a), its concentration at the interface c_i can be assumed to remain constant at $c_{i,max}$ (Schaffer et al. 2013; Tatomir et al. 2018). Thus, the originally first order hydrolysis reaction can be simplified into a pseudo zero-order reaction, which can be expressed with Eq.(3):

$$R_{c_{n\to w}} = \frac{M^k_{n\to w}}{A_{wn} \cdot \Delta t} \tag{3}$$

where $R_{c_{n\to w}}$(kg·s^{-1}m^{-2}) is the reaction rate of the KIS tracer per unit interfacial area, $M^k_{n\to w}$(kg) is the mass of the reaction product k, Δt is the reaction time, and A_{wn} is the FIFA (m^2). In a series of batch experiments $R_{c_{n\to w}}$ was determined at 2.95×10^{-12}kg·s^{-1}m^{-2} (Tatomir et al. 2018). From Eq.(3) it is obvious that the mass transfer rate is only controlled by the magnitude of the FIFA. The two reaction products are naphthalene-2-sulfonic acid (2-NSA) and phenol, both measurable in the water phase samples. Tatomir et al. (2018) and Schaffer et al. (2013) showed in static batch experiments with the FIFA kept constant, that the 2-NSA is the compound more easily measured in a tracer experiment because of its enhanced fluorescence (2-NSA concentration in the order of μgL^{-1}). With 2-NSA characterized by high polarity i.e. highly hydrophilic, it will be distributed into the bulk water (here also the wetting phase) away from the interface. The high water solubility explains a negligible back-partitioning. Static batch experiments showed a linear increase of the 2-NSA concentration in water (Tatomir et al. 2018). Furthermore, the adsorption of 2-NSA on water-solid interfaces has not been observed to have any visible effect on mass transport in previous laboratory studies, and thus it is not considered further (Schaffer et al. 2013; Tatomir et al. 2018). With a zero-order reaction at the interface, numerical modeling of 2-NSAPh decay and transport in the non-wetting phase becomes redundant, and the most relevant component of mass transport modeling is the

reaction product 2-NSA, present only in the wetting phase. On the pore-scale, modeling of the hydrolysis reaction and the 2-NSA transport imply several main steps: 1) zero-order reaction, which is equivalent to a constant production of 2-NSA at the interface, 2) distribution of produced 2-NSA in the water phase controlled by molecular diffusion and high water solubility, and 3) transport of 2-NSA in the water phase controlled by advection and molecular diffusion.

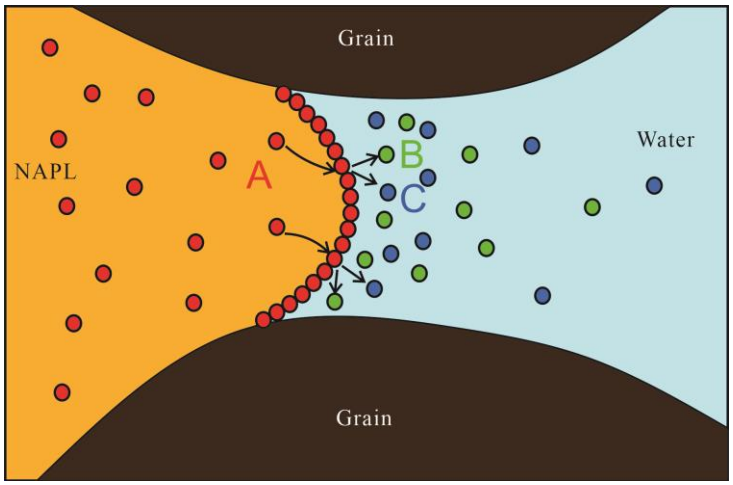

Figure 1 Schematic of the KIS tracer reactive transfer process (after Tatomir et al. 2018). A: Phenyl Naphthalene-2-Sulfonate. B: Naphthalene-2-Sulfonic Acid. C: Phenol.

The potential of applying KIS tracers in real porous media to determine the FIFA under dynamic conditions was first demonstrated by Tatomir et al. (2018). Tatomir et al. (2018) provided a proof-of-concept using controlled column experiments with well-characterized porous media composed of glass beads. The KIS tracers were dissolved in a NAPL (n-octane) to displace the water in, initially, fully saturated columns. At the column outlet, measurements of fluid volume and 2-NSA concentration of the samples collected at defined time intervals provided breakthrough curves (BTCs) of fluid volumes and the 2-NSA concentration in the water phase. The analysis of the experimental data was conducted employing a macro-scale, reactive, two-phase flow and transport model (Tatomir et al. 2015; Tatomir et al. 2016b; Tatomir et al. 2018; Tatomir et al. 2019; Tatomir et al. 2020), with the interfacial reaction of the tracer being specified in the unsaturated zones with both fluids co-existing, and the FIFA approximated explicitly as a function of saturation. The model predicted a nearly linear concentration BTC which could fit most of the experimental data points. The resulting specific FIFA (defined as the interfacial area per unit volume of porous medium) ranged between 500-750m^{-1} for glass beads with a mean diameter of 240μm. Despite the successful application of the KIS tracers in laboratory column experiments, new questions came up, such as: a) what is the FIFA the tracers actually measure, i.e., capillary associated, b) how much 2-NSA will end up in the water-film coating the grains and in the hydro-dynamically stagnant zones, and c) how do these stagnant zones influence the resulting BTC?

142 The stagnant zones, also referred to as the immobile zones, for the porous media flow
143 are defined as the region where flow velocity is very weak and mass transport
144 becomes diffusive (van Genuchten and Wierenga 1976; Karadimitriou et al. 2016).
145 The experimental study at column scale found that the presence of immobile zones
146 can affect the BTCs of the tracer in two-phase flow systems, i.e. larger longitude
147 dispersion, early breakthrough and long tailings (Smedt and Wierenga 1984; Bond
148 and Wierenga 1990; Khan and Jury 1990; Bromly and Hinz 2004). The pore-scale
149 micro-model experiments studying the development, the role and importance of
150 immobile zones was first conducted by Karadimitriou et al. (2016), who found a
151 nonlinear contribution of the immobile zone to the dispersion coefficient and a non-
152 monotonic relation between immobile zone saturation and total saturation under
153 transient transport conditions. Karadimitriou et al. (2017) further studied the impact of
154 Péclet number under several given saturation topologies, and they found that the ratio
155 of immobile zone saturation to total saturation is not influenced by the different flow
156 rates. Hasan et al. (2019) confirmed these findings with pore-network modeling, and
157 they found a linkage between the immobile zone saturation with the relative
158 permeability. The flaws of existing macroscopic models to describe the non-Fickian
159 transport in two phase flow process were proposed in these recent studies
160 (Karadimitriou et al. 2016; Karadimitriou et al. 2017; Hasan et al. 2019). In contrast
161 to these studies with a conservative tracer injected simultaneously with the invading
162 phase, the KIS tracer dissolved in the invading phase depends on the hydrolysis
163 reaction at the interface and the detection of the by-product in the receding phase.
164 This means, in our case, the effect of immobile zones is manifested in the solute
165 transport in the receding phase.

166

167 The above questions, regarding the effect of the immobile zones on the distribution of
168 the reacted solute in KIS-TT, can probably be answered by investigating KIS tracer
169 transport mechanisms at the pore-scale. Two possible alternatives are available. The
170 pore-scale study of KIS tracer reactive transport in two- phase flow can be carried out
171 experimentally e.g., as in micro-models (Karadimitriou et al. 2016), considering its
172 good fluorescent properties, as well as, by pore-scale modeling. Pore-scale modeling
173 plays an important role in understanding the pore-scale phenomena and can provide
174 fundamental insight to understand the macro-scale processes (Meakin and
175 Tartakovsky 2009). With pore-scale modeling, the flow and transport properties of the
176 soil/ rock matrix are not averaged but are directly resolved, and the pore-space
177 geometry is explicitly represented either by using idealized geometries or by
178 reconstructed geometries based on XMT images (e.g., Culligan et al. 2004; Tatomir et
179 al. 2016a; Peche et al. 2016). In addition, running pore-scale simulations is a more
180 flexible approach than the experiments since there is freedom to tune accordingly the
181 fluids' physical and chemical properties, and the geometry of the porous medium for a
182 variety of boundary conditions. Considering all the above, the main objective of this
183 study is to develop a pore-scale model that can simulate the behavior of the reactive
184 KIS tracer transport under two-phase flow conditions. The following sections review
185 the relevant literature on pore-scale models including reactive transport.

186

1.2Pore-scale numerical methods

Pore-scale modeling methods mainly include Pore-Network Modeling (PNM) and Direct Numerical Simulation (DNS) approaches. The DNS approaches include particle-based methods e.g. the Lattice Boltzmann Method (LBM), Smooth Particle Hydrodynamics (SPH), and grid based Computational Fluid Dynamics (CFD), such as the Level-Set Method (LSM), the Volume-Of-Fluid method (VOF), and the Phase-Field Method (PFM) (Meakin and Tartakovsky 2009; Alpak et al. 2016). Pore-Network Modeling (PNM) is a well-developed method for pore-scale studies (Blunt and King 1990; Joekar-Niasar et al. 2008; Raoof et al. 2013; Hasan et al. 2019). PNM simplifies porous media into networks of pores and throats, where flow is governed by Poiseuille's law (Joekar-Niasar et al. 2008). PNM is computational more efficient than DNS, which providing the full coupling between capillary and viscous forces (Alpak et al. 2016). With PNM, it is computationally cheaper to consider domains with a size large enough to be considered as Representative Elementary Volumes (REVs), and thus the model can be applied for evaluation of continuum-scale problems. Despite these advantages, PNM is limited by its basis on simplified physics and simplified representations of the rock (Meakin and Tartakovsky 2009; Alpak et al. 2016; Basirat et al. 2017; Yin et al. 2019). Thus, the DNS methods, based on first principles, is better for capturing transport phenomena and fluid dynamics on the micro-scale, in (real) pore space with complex geometries (Meakin and Tartakovsky 2009; Alpak et al. 2016). The LBM is a popular method for pore-scale studies of multiphase reactive transport, because of its advantages in several aspects, such as being able to deal with complex boundaries, to incorporate microscopic fluid-fluid and fluid-solid interactions, and being able to implement a parallelization of the algorithm (Kang et al. 2006b; Liu et al. 2014; Liu et al. 2015). The LBM model solves the LB equations for fluid flow and solute transport. In LB simulations the chemical reaction of species is treated as a homogenous reaction in the bulk fluid and a heterogeneous reaction at the interface as a kinetic boundary condition. The LBM modelling approach has been used in applications such as geological storage of CO_2, which involves precipitation and dissolution at the fluid-solid surface (Kang et al. 2010) and CO_2 dissolution trapping (Chen et al. 2018). However, one of the disadvantages of the LBM models is that the relation between interaction forces and fluid dynamics requires complex calibration procedures, with many adjustment parameters such as the adequate approximation of a specific physical system (Ferrari and Lunati 2013; Frank et al. 2018). With the CFD approach, the Navier-Stokes equations are directly solved in a discretized domain by finite volume or finite element techniques, and the interface between two fluids is represented by an indicator function, such as the volume fraction in VOF and the phase variable in PFM. One challenge for the simulation of multiphase reactive transport with the CFD method is the handling of the concentration jump at the interface when a solute solubility is different in the fluids on either side of the interface (Maes and Soulaine 2018). Haroun et al. (2010) managed to tackle this challenge with a new Continuous Species Transfer (CST) formulation developed in the VOF framework. In the CST formulation, a constant partition coefficient (or Henry's constant) is introduced to solve the thermodynamic equilibrium of the solute at the interface between two fluids (Haroun et al. 2010). The approach of Haroun et al. (2010) allows for the modeling of the discontinuous solute concentration across the interface, while respecting the continuity of the local diffusive solute mass flux. Graveleau et al. (2017) applied the VOF-CST model to simulate subsurface flow problems with moving contact lines. Maes and Soulaine (2018) identified that the CST generates large numerical diffusion

in the phase concentration, which leads to inaccurate simulation of solute mass between two phases. Therefore, they proposed a new approach, termed compressive CST (C-CST), by adding a compressive term. The C-CST formula managed to significantly reduce numerical errors. However, one major disadvantage of the VOF method is that, since the volume fraction is a step function, accurate curvature and smooth physical quantities near the interface are hard to be obtained (Sun and Tao 2010; Alpak et al. 2016). Another limitation of the VOF method is that a solid wall boundary is implemented indirectly with an additional moving contact line model (Meakin and Tartakovsky 2009; Basirat et al. 2017).

In contrast to the VOF method, LSM and PFM with a smooth indicator function are better to treat the curvature and the physical quantities at the interface. LSM has been reported to generate more numerical errors when the interface experiences severe stretching or tearing, and the mass is not conserved (Sussman and Puckett 2000; Sun and Tao 2010). Major advantages of PFM are both the mass conservation and the ability to compute accurately the curvature at the interface (Akhlaghi Amiri and Hamouda 2013). Furthermore, PFM treats the interface thermodynamically as a diffuse thin layer formed by the mixture of the two fluid phases, and the dynamics of the diffuse interface is governed by the free energy it contains (Yue et al. 2006). Thus, the PFM is physically more consistent than the VOF or the LSM models (Alpak et al. 2016). Another advantage is that considering a diffusive interface rather than a sharp interface around the contact line results effectively in slip, through the diffusive fluxes between the bulk fluids (Ding and Spelt 2007). Besides, with a diffusive interface in PFM, the zero-order reaction of 2-NSA at fluid-fluid interface can be directly implemented as a homogenous reaction in the region of the diffusive interface, where the two phase fluids mix. The PFM, solving the coupled Cahn-Hilliard and Navier-Stokes equations, is already well developed and numerous simulation studies were performed addressing the two-phase flow system (Jacqmin 1999; Yue et al. 2004; Yue et al. 2006; Akhlaghi Amiri and Hamouda 2013; Alpak et al. 2016). In addition, numerous recent studies have applied PFM to study various subsurface flow problems related to fluid viscosity, capillarity, temperature, wettability, heterogeneity and fractures (Akhlaghi Amiri and Hamouda 2013, 2014; Basirat et al. 2017; Rokhforouz and Akhlaghi Amiri 2017, 2018). To our knowledge, PFM has not yet been applied to study reactive transport for two phase flow in porous media.

Here, we derive a new CST formulation in a PFM framework, and therefore the model is termed PFM-CST. First, we verify the developed PFM-CST model, and second, we employ the code to study KIS tracer reaction and transport processes in immiscible two-phase flow in porous media. We then demonstrate the capability of the model to investigate the relative importance of different processes and different parameters in two-phase flow reactive transport simulations. We focus on the understanding of how fluid immobile zones affect the magnitude of total transported solute mass. The paper is organized as follows: Section 2 introduces the mathematical and numerical models. In Section 3 we present the verification and validation of the model, and its application to a realistic pore space geometry to study the KIS tracer reaction and transport of its reaction by-product 2-NSA. Section 4 lists the main conclusions.

2. Mathematical model

2.1Phase-Field Method

The basics of the PFM can be found in e.g., Jacqmin (1999), Yue et al. (2004) and Alpak et al. (2016). In this section, we briefly review the basic underlying theory implemented in the model. Instead of a sharp interface between two fluids, the PFM treats the interface as a thin diffusive layer formed by the mixture of two fluids. The PFM introduces a smoothly changing phase variable ϕ to describe the composition of the fluid mixture at the interface, and ϕ remains constant in the bulk fluid phases. The PFM is based on of the free energy density as a function of the phase variable and its gradient (Jacqmin 1999). The free energy density (f_{mix}) for isothermal mixing of two fluids can be expressed in the Ginzburg-Landau form (Eq.(4)) (Yue et al. 2006):

$$f_{mix}(\phi, \nabla\phi) = \frac{1}{2}\lambda|\nabla\phi|^2 + \frac{\lambda}{4\varepsilon^2}(\phi^2 - 1)^2 \tag{4}$$

where λ is the magnitude of the mixing energy and ε is a capillary width representing the thickness of the diffusive interface. The free energy density is made up of two components (on the right side of the Eq.(4): the first term accounts for the surface energy and the second term is the bulk energy. The surface energy describes the preference of both fluids to blend. The bulk energy describes the two-phase immiscibility and involves two minimal values, where ϕ=1 and ϕ=-1, representing the two bulk phases (wetting and non-wetting fluid), respectively (Jacqmin 1999). These two competing energies determine the ϕ profile across the interface (Jacqmin 1999; Yue et al. 2004). The chemical potential G can be defined as the variation of the free energy with respect to the phase variable (Eq.(5)):

$$G = \frac{\delta \int_{-\infty}^{+\infty} f_{mix}\, dx}{\delta\phi} = -\lambda\nabla^2\phi + \frac{\lambda}{\varepsilon^2}\phi(\phi^2 - 1) \tag{5}$$

At equilibrium with zero chemical potential G=0, the equilibrium profile in 1D for φ(x) writes (Eq.(6)):

$$\phi(x) = tan\, h\left(\frac{x}{\sqrt{2}\varepsilon}\right) \tag{6}$$

The total free energy at the interface is the surface tension σ, and the relationship between the surface tension, the capillary width, and the mixing energy density can be obtained at equilibrium from Eq.(7) (Yue et al. 2004):

$$\sigma = \frac{2\sqrt{2}\lambda}{3\varepsilon} \tag{7}$$

Fluid mass conservation is governed by the Cahn-Hilliard equation (Eq.(8)), which assumes that the diffusive fluid flux is proportional to the gradient of the chemical potential (Cahn and Hilliard 1959):

$$\frac{\partial\phi}{\partial t} + \mathbf{u}\cdot\nabla\phi = \nabla\cdot(\gamma\nabla G) \tag{8}$$

where γ is the mobility expressed as a function of the interface thickness and a tuning factor: $\gamma = \chi\cdot\varepsilon^2$. The tuning factor χ is called the characteristic mobility governing the relaxation time of the interface (Akhlaghi Amiri and Hamouda 2013). X needs to

be large enough to maintain a constant thickness of the interface, but small enough not to dampen the flow (Jacqmin 1999).

2.2Two phase flow dynamics

Momentum conservation for an incompressible fluid is governed by the Navier-Stokes equation (Eq.(9)):

$$\rho\left(\frac{\partial u}{\partial t}+\mathbf{u}\cdot\nabla\mathbf{u}\right)=\nabla\cdot[-p\mathbf{I}+\mu(\nabla\mathbf{u}+(\nabla\mathbf{u})^{T})]+G\nabla\phi+\rho\mathbf{g} \tag{9}$$

$$\rho\cdot\nabla\mathbf{u}=0 \tag{10}$$

where **I** is the identical tensor, p is pressure, **u** is the fluid velocity vector, **g** is the gravity vector, the surface tension is considered as a body force (Yue et al. 2006),

$$-\frac{\delta\int f_{mix}\,d\Omega}{\delta x}=\ G\nabla\phi \tag{11}$$

and ρ and μ are respectively the density and viscosity of the mixture (non-wetting fluid and wetting fluid) according to volume fraction of the fluids:

$$\rho=\rho_w V_{f,w}+\rho_{nw}V_{f,nw}\text{ and }\mu=\mu_w V_{f,w}+\mu_{nw}V_{f,nw} \tag{12}$$

where subscripts *w* and *nw* indicate wetting and non-wetting phase, respectively. The volume fraction of the fluids can be obtained as:

$$V_{f,w}=(1-\phi)/2\text{ and }V_{f,nw}=(1+\phi)/2 \tag{13}$$

At the grain surfaces, a no-slip boundary is applied, which implies that **u**=0 in Eq.(9) for solid wall boundaries. The wetting condition on the solid wall is expressed by Eq.(14):

$$n\cdot\nabla\phi=cos\theta_w|\nabla\phi| \tag{14}$$

where **n** is the (outward) normal vector to the wall and θ_w is the contact angle.

2.3 Reactive transport

2.3.1 Advection-diffusion equation

To obtain the solute mass conservation equation, Eq. (8) is rewritten by replacing the phase variable with the volume fraction of phase α $V_{f,\alpha}$, as:

$$\frac{\partial V_{f,\alpha}}{\partial t}+\mathbf{u}\cdot\nabla V_{f,\alpha}-\frac{dV_{f,\alpha}}{d\phi}\cdot\nabla\cdot(\gamma\nabla G)=0 \tag{15}$$

Hence, for the solute k in fluid phase α, the advection-diffusion equation writes:

$$\begin{aligned}\frac{\partial(V_{f,\alpha}c_{\alpha,k})}{\partial t}+\nabla\cdot(\mathbf{u}\cdot V_{f,\alpha}\cdot c_{\alpha,k}-\frac{dV_{f,\alpha}}{d\phi}\gamma\nabla G\cdot c_{\alpha,k})\\=\nabla\cdot(D_{\alpha,k}\nabla c_{\alpha,k})+W_k\end{aligned} \tag{16}$$

where $c_{\alpha,k}$ is the concentration of the solute k in the fluid phase α. The second term on the left side of Eq.(16) describes the solute transport due to the bulk fluid motion. The bulk fluid motion consists of two parts: the advective flux and the diffusive flux at the

interface due to the gradient of the chemical potential. On the right hand side of the Eq.(16), $D_{a,k}$ is the molecular diffusion coefficient of solute k in fluid phase α given by Fick's law. W_k is the source term for mass generated by chemical reactions.

2.3.2Reaction at the interface

A zero-order interfacial reaction of the KIS tracer is assumed in the model as a homogeneous reaction taking place at the diffusive interface, where the two fluids mix. The diffuse interface is the region with $\phi \in$(-1,1), and due to the smooth change in ϕ there is no clear boundary of the diffuse interface. Thus, we take the interface with 90% variation of the phase variable $\phi \in$[-0.9,0.9] or $V_{f,w} \in$[0.05,0.95] as the region of constant zero-order reaction. It is worth noting that the reaction source term applied here is discontinuous. With the constant interface thickness, the reaction rate per unit interfacial region for the model can be calculated as:

$$W_k = R_c^{dif} = \frac{R_{c_{n\to w}}}{b_{wn}} \tag{17}$$

Where $R_{c_{n\to w}}$ is the experimental determined tracer reaction rate per unit interfacial area (Tatomir et al. 2018), and b_{wn} is the thickness of interfacial reaction region with $V_{f,w} \in$[0.05,0.95], obtained as 4.1641ε from Eq.(6).

2.3.3 Solute distribution across the interface

As mentioned in the introduction, the reaction product (2-NSA) has high water solubility and distributes homogeneously into the water phase. This selective distribution mechanism is not included in the classical advection-diffusion equation. In this case, we applied the method developed by (Haroun et al. 2010), where a partitioning coefficient is introduced in the formulation. The partitioning coefficient is expressed as the concentration ratio of the solute in the two-phase fluids system at equilibrium.

$$P_{ow,k} = \frac{c_{nw,k}}{c_{w,k}} \tag{18}$$

where $c_{nw,k}$ and $c_{w,k}$ are the concentration of the product (2-NSA) in the non-wetting phase and the wetting phase respectively, and $P_{ow,k}$ is the partition coefficient. The octanol/water partition coefficient of 2-NSAis equal to logDow=-2.87 at PH>5, as stated in the work of (Schaffer et al. 2013).

2.3.4Continuous transport equation

To obtain the single-field formulation of the (2-NSA) concentration for both phases in the entire domain, we define the global concentration as:

$$c_k = V_{f,w} c_{w,k} + V_{f,nw} c_{nw,k} \tag{19}$$

The sum of the mass conservation Eq.(16) for solute k in both phases resulting in the conservation of global concentration writes:

$$\frac{\partial c_k}{\partial t} + \nabla \cdot F_k = \nabla \cdot J_k + W_k \tag{20}$$

where

$$F_k = \mathbf{u} \cdot c_k + \left(c_{w,k} - c_{nw,k}\right) \cdot 0.5\gamma \nabla G \tag{21}$$

374

$$J_k = D_k \cdot (V_{f,w} \nabla c_{w,k} + V_{f,nw} \nabla c_{nw,k}) = D_k [\nabla c_k + \left(c_{w,k} - c_{nw,k}\right) \nabla V_{f,w}] \tag{22}$$

375 As $V_{f,w} + V_{f,nw} = 1$, here only $V_{f,w}$ is used in the expression, and the diffusivity is
376 expressed as $D_k = V_{f,w} D_{w,k} + V_{f,nw} D_{nw,k}$. The diffusion term Eq.(22) indicates an
377 additional flux term resulting from the solubility law. This solubility flux is in
378 direction normal to the interface, which governs the distribution of the species
379 between the two phases. With the definition of Eq.(18) and Eq.(19), one obtains:

$$c_{w,k} - c_{nw,k} = \frac{c_k (1 - P_{ow,k})}{V_{f,w} + P_{ow,k} (1 - V_{f,w})} \tag{23}$$

380 Thus, the final governing equation for global concentration of solute *k* is reorganized:

$$\begin{aligned} &\frac{\partial c_k}{\partial t} + \nabla \cdot (\mathbf{u} c_k) + \nabla \cdot \left(0.5\gamma \nabla G \frac{c_k \left(1 - P_{ow,k}\right)}{V_{f,w} + P_{ow.k} \left(1 - V_{f,w}\right)}\right) \\ &\qquad = \nabla \cdot \left(D_k \left(\nabla c_k + \nabla V_{f,w} \frac{c_k \left(1 - P_{ow,k}\right)}{V_{f,w} + P_{ow,k} \left(1 - V_{f,w}\right)}\right)\right) + W_k \end{aligned} \tag{24}$$

381 **2.4 Numerical implementation**

382 The model is implemented into COMSOL Multiphysics™. COMSOL is an
383 interactive environment for simulating different scientific and engineering problems
384 employing the finite element method for spatial discretization (Akhlaghi Amiri and
385 Hamouda 2013; Tatomir et al. 2018). The governing system comprises four governing
386 equations and four fundamental variables. The coupled governing equations of the
387 Navier-Stokes equation (Eq.(9) and Eq.(10)) and the Cahn-Hilliard equation (Eq.(8))
388 are solved for fluid velocity (**u**), pressure (p) and the phase variable (ϕ). And the
389 governing reactive transport equation (Eq.(24)) is solved for the solute concentration
390 (c_k). The partial differential equations are solved by the COMSOL linear solver
391 PARDISO. Time stepping is solved with the backward Euler method known for its
392 stability. The initial time step and maximum time steps are controlled to be small
393 enough in order to avoid a singularity. The mesh elements consist of regular triangles
394 with side length h. The mesh size is refined according to the complexity of the
395 geometry and thickness of the interface. The computations were performed on a
396 single CPU with 12 cores at 4.3 GHz, and 32 GB RAM.

397 # 3. Numerical Method and details

398 We first validate the reactive transport model by applying the newly implemented
399 continuous transport algorithm (Eq.(24)) (section 3.1). Then, the model is tested for a
400 drainage process in a capillary tube (section 3.2). Finally, the model is applied to
401 study the KIS tracer reactive transport in a realistic 2D porous medium geometry
402 proposed by Keller et al. (1997)(section 3.3).

403

3.1 Model validation and verification

For the model validation and verification, we provide first validations of the two-phase flow simulation with the phase-field method. The two-phase flow model is validated and verified in two different cases: a pressure difference driven, co-current two-phase flow through a thin channel (Appendix A1) and a surface tension driven, deformed bubble retraction process in a quiescent domain (Appendix A2). The important parameters for phase-field method, such as characteristic mobility, capillary width and mesh size, are studied. Besides, since the model is to be employed to simulate two-phase flow and reactive transport in porous materials, the phase distribution in the regions close to the grain surface needs to be resolved by the model in detail. Thus, we set up a benchmark simulation of the deposited water films on the grain surface (Appendix A3). Then, we provide a verification of the reactive transport simulation governed by the above Eq.(24). Since solute advection depends on the bulk fluid motion calculated from the two-phase flow model, emphasis on the verification for the reactive transport model is placed on the remaining mechanisms, such as the reaction at the interface and molecular diffusion. The verification is accomplished by comparing the results of the numerical model with those of an analytical solution for a transient interfacial diffusion process (section 3.1.1) and a simultaneous reaction-diffusion process at the interface (section 3.1.2).

3.1.1 Diffusion across the interface

When a solute dissolves in a two-phase fluid system with non-equal solubilities in each fluid phase, a concentration jump will be formed at the interface at equilibrium, assuming this interface is a sharp one. In this section, we study how this concentration jump is dealt with for a diffusive interface by the model. We consider a simple two-phase system without any reaction, and only the wetting phase contains the chemical component 2-NSA initially. The model is setup in 1D as follows: in a 0.2mm long domain, the interface is located at x=0.1mm. Water is located at x>0.1mm and the non-wetting phase is located at x<0.1mm, as shown in **Figure 2**(a). The system is at rest without any inflow or outflow. Water has an initial solute (2-NSA) concentration of $c_{w,0}$=1 mol/m^3, and the non-aqueous, or non-wetting, phase has an initial solute (2-NSA) concentration $c_{nw,0}$=0. Diffusivity is D_w=D_{nw}=1×10^{-9}m^2/s for both phases. With this modeling setup, solute diffusion across the interface is allowed to take place. This transient diffusion process can be described by the analytical solution from Eq.(25) for water and Eq.(26) for the non-wetting phase (Bird 2002):

$$\frac{c_w - c_{w,0}}{c_{nw,0} - P_{ow} \cdot c_{w,0}} = \frac{1 + erf\left[\frac{x-0.1}{\sqrt{4D_w t}}\right]}{P_{ow} + \sqrt{D_w/D_{nw}}} \tag{25}$$

$$\frac{c_{nw} - c_{nw,0}}{c_{w,0} - \left(\frac{1}{P_{ow}}\right) \cdot c_{nw,0}} = \frac{1 - erf\left[\frac{x-0.1}{\sqrt{4D_{nw} t}}\right]}{\left(\frac{1}{P_{ow}}\right) + \sqrt{D_{nw}/D_w}} \tag{26}$$

where erf( ) is the error function. The system with very small partition coefficient is the focus of our study, as the 2-NSA has P_{ow}<0.01, which means it has very small partition into the non-wetting phase.

Then, we provide a verification of how solute distribution is treated at the diffusive interface. With the very low partitioning coefficient (P_{ow}<0.01), the solute concentration in water is much larger than that in the non-wetting phase $c_{w,k}$>>$c_{nw,k}$. And the solute concentration in water almost remains at $c_{w,k}$=1 mol/m^3 because of the weak diffusion across the interface and the absence of the chemical reaction. In this case, Eq.(19) can be simplified to $c_k = V_{f,w}c_{w,k}$. This means that the solute concentration of the mixture (c_k) at the interface is approximately linearly proportional to the volume fraction of the water phase ($V_{f,w}$), with a ratio of $c_{w,k}$. By comparing the simulated concentration curve to the corresponding volume fraction of the fluid, we are able to check if the solute concentration distribution at the diffuse interface is accurately solved by the model.

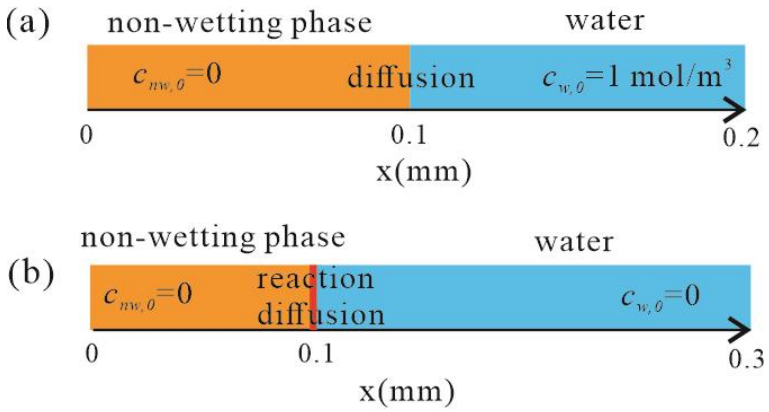

Figure 2 Sketch of the numerical setups for verification of the reactive transport model in (a) a transient interfacial diffusion process and (b) a simultaneous reaction-diffusion process at the interface.

3.1.2 Interfacial reaction and molecular diffusion

The model is verified for the condition that a zero-order reaction is active. We consider a one-dimensional quiescent channel with two phase fluids. The solute is assumed to react at the interface and diffuse into the water. The channel is 0.3mm in length, with the interface located at x=0.1mm. The water is located at x>0.1mm and the non-wetting phase (n-octane) is located at x<0.1mm, as shown in **Figure 2**(b). The initial 2-NSA concentration in the domain is c_0=0 mol/m^3. The diffusivity is equal to D=1×10^{-9}m^2/s for both phases. The zero-order reaction rate is W=R_c^{dif} =1 mol/m^{-2}s. The capillary width for the model is set at ε=1×10^{-7}m, thus the reaction region at the interface has a thickness of 4.16ε according to section 2.3.2.

The above process can be described by the reaction-diffusion equation:

$$\partial c/\partial t = \nabla \cdot (-D\nabla c) + W \tag{27}$$

which can be solved analytically. For the analytical solution, the interface between two phases is defined as a no flow boundary for the solute, and the zero-order reaction is active in a narrow region with 0.1mm<x<L. The analytical solution for Eq.(27) is shown below (Carslaw and Jaeger 1959):

475 At $0.1mm < x < L$

$$c = R_c \cdot t \cdot \left\{1 - 2i^2erfc\frac{L - x + 0.1}{2\sqrt{D \cdot t}} - 2i^2erfc\frac{L + x - 0.1}{2\sqrt{D \cdot t}}\right\} \quad (28)$$

476 At $x > L$

$$c = 2R_c \cdot t \cdot \left\{i^2erfc\frac{L - x + 0.1}{2\sqrt{D \cdot t}} - i^2erfc\frac{L + x - 0.1}{2\sqrt{D \cdot t}}\right\} \quad (29)$$

477 where$i^2erfc\ x = 0.25[(1 + 2x^2)erfc\ x - 2xe^{-x^2}/\sqrt{\pi}]$, erfc is the complementary
478 error function, and L is the thickness of the reaction region for the analytical solution.
479 To be consistent with the model, the thickness of reaction region is set as L=4.16ε.

480

481 **3.2 Model test in a capillary tube**

482 The model is tested for the relevant processes (reaction, two-phase flow, advection
483 and diffusion) in a single two-dimensional capillary tube setup. We focus on the effect
484 of fluid flow (advection) and molecular diffusion on the transport of solute for a
485 spectrum of Péclet numbers. The tube is 0.8mm long with a radius of R=0.05mm, and
486 in 2D the top and bottom boundaries are the solid walls accounting for the pore space
487 surface. The tube is initially filled with water and n-octane is injected from the left
488 side with a constant velocity of U_{in}=0.05m/s at t=0. The contact angle between the
489 two fluids and the boundary wall is set to 45°. The interfacial tension for n-
490 octane/water is equal to σ=0.0504 N/m (Tatomir et al. 2018), and R_c^{dif} =1mol/m^{-2}s.
491 The Péclet number for the system is calculated as: $Pe = u * L_c/D$, where L_c is the
492 characteristic length, in this case equal to the radius of the capillary L_c=R. As the L_c is
493 fixed, the Péclet number of the systems is determined by the ratio between the inflow
494 rate and diffusivity. To obtain the systems with different Péclet numbers, we maintain
495 the inflow rate and swap the diffusivities with D=1×10^{-8}m^2/s, D=1×10^{-7}m^2/s and
496 D=1×10^{-6}m^2/s in three simulations.

497

498 **3.3 Model application for flow in porous media**

499

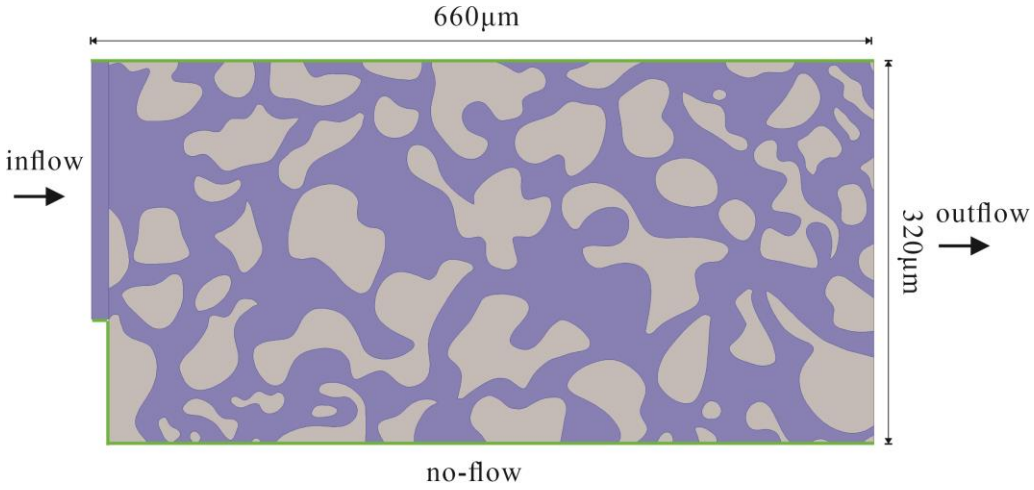

Figure 3 Geometry of the porous medium and boundary conditions (pore space in blue color).

We applied the PFM-CST model to study KIS tracer reactive transport in a hydrophilic 2D porous medium. The focus of the study is to verify the model by analyzing the quantified macroscopic parameters, e.g. saturation, capillary pressure, specific interfacial area, solute concentration, and to understand the effect of the induced immobile zones on transport of the reaction product (2-NSA). We assumed a 2D porous medium from a thin slice of Berea sandstone, first presented by Keller et al. (1997) for a micro-model experiment. The geometry has already been used as the computational domain in Basirat et al. (2017) and Rokhforouz and Akhlaghi Amiri (2019). The domain measures 660μm×320μm in size, and consists of an extensive rectangular (inflow) used to inject the fluids on the left side, and the actual porous medium domain, as shown in **Figure 3**. The porous medium is initially saturated with water, and n-octane with dissolved KIS tracer is injected from the left boundary with a constant velocity U_{in}. The right-hand side of the domain is the outlet, and the upper and lower sides of the domain are no flow boundaries. The relevant parameters of the non-wetting fluid are ρ_{octane}=703kg/m^3 and μ_{octane}=0.54×10^{3}Pa·s, and interfacial tension for n-octane/water σ=0.0504 N/m. With the solution of the reaction-diffusion equation Eq.(28) and Eq.(29), we know that the zero-order reaction rates can only influence the magnitude of the resulting solute concentration curves, but not its shape. This means that the reaction rate does not affect solute transport, and transport of the solute depends on its diffusivity and the bulk fluid motion. As the study focus on providing an understanding of the transport and the distribution of the tracer, and the result is not compared to a real experiment where solute concentration needs to be calibrated, here we use a unit reaction rate of R_c^{dif}=1mol/m^{-2}s. Time is expressed in a dimensionless form with the characteristic time, meaning the time needed for breakthrough when the porous media is equivalent to a capillary tube being $t_c = L_c/U_{in}$, where L_c is the characteristic length, and is equal to the length of the domain L_c=0.66mm. Changes in the parameters of the flow system, e.g., capillary number, Péclet number, contact angle, influence the transport process of the KIS tracer and its reaction products. To better understand the influence of these parameters we conduct four simulations, changing one parameter at a time, i.e., inflow velocity, diffusivity and contact angle. The parameters for each case study are listed in **Table 1**. The capillary number is calculated as: $Ca = U_{in} \cdot \mu_{nw}/\sigma$.

Table 1 Parameters for the simulations and resulting dimensionless numbers, Ca.

	U_{in}(m/s)	D (m^2/s)	θ_w(°)	Ca
Case 1	0.05	1e-8	45	5e-4
Case 2	0.05	1e-7	45	5e-4
Case 3	0.05	1e-7	15	5e-4
Case 4	0.01	1e-7	45	1e-4

4. Results and discussion

We first show the result of the model validation in section 4.1. Then, the results of simulating the capillary drainage are shown in section 4.2. Finally, the results of model application to study the KIS tracer reactive transport in a realistic 2D porous medium geometry are shown in section 4.3.

4.1 Model validation

Simulation results are shown and compared with analytical solutions, for a transient interfacial diffusion process in section 3.1.1, and for a simultaneous reaction-diffusion process at the interface in section 3.1.2.

4.1.1 Diffusion across the interface

The transient diffusion process depends on the partition coefficient of the solute. **Figure 4**(a) shows the comparison between breakthrough calculated by the analytical solution at t=0.5s for P_{ow}=1, P_{ow}=0.1, P_{ow}=0.01 and P_{ow}=0.001 and that of the numerical model. It is found that the model results match those of the analytical solution well. With a lower partition coefficient, solute partitioning into the non-wetting phase is less. When P_{ow}<0.01, the diffusion across the interface has already become very small. The extremely small value of P_{ow} will cause instability of the model. Thus, P_{ow}=0.01 is applied for 2-NSA in this study. **Figure 4**(b) shows the resulting concentration profiles near the interface at t=0.5s. The solid curve shows the analytical solution considering a sharp interface. The Cahn number indicates the thickness of the interface: $Cn = \varepsilon/L_c$, where L_c is the characteristic length that equals the length of the domain L_c=0.2mm. The dashed curves show the modeling results at Cn=5×10^{-3} and Cn=5×10^{-4}. It shows that with a thicker interface, the deviation from the sharp interface solution becomes larger, as expected. Besides, the modeled concentration curves (in dashed lines) smoothly changing across the diffusive interface, which is different from the analytical solution and its discontinuous concentration profile for the sharp interface. We plot the corresponding volume fraction of water in the second y-axis (with scale on the right side) in **Figure 4**, and it is found that the concentration curve fits the corresponding volume fraction curves. This proves that the 2-NSA concentration is simulated accurately by the model for a mixture condition at the diffuse interface.

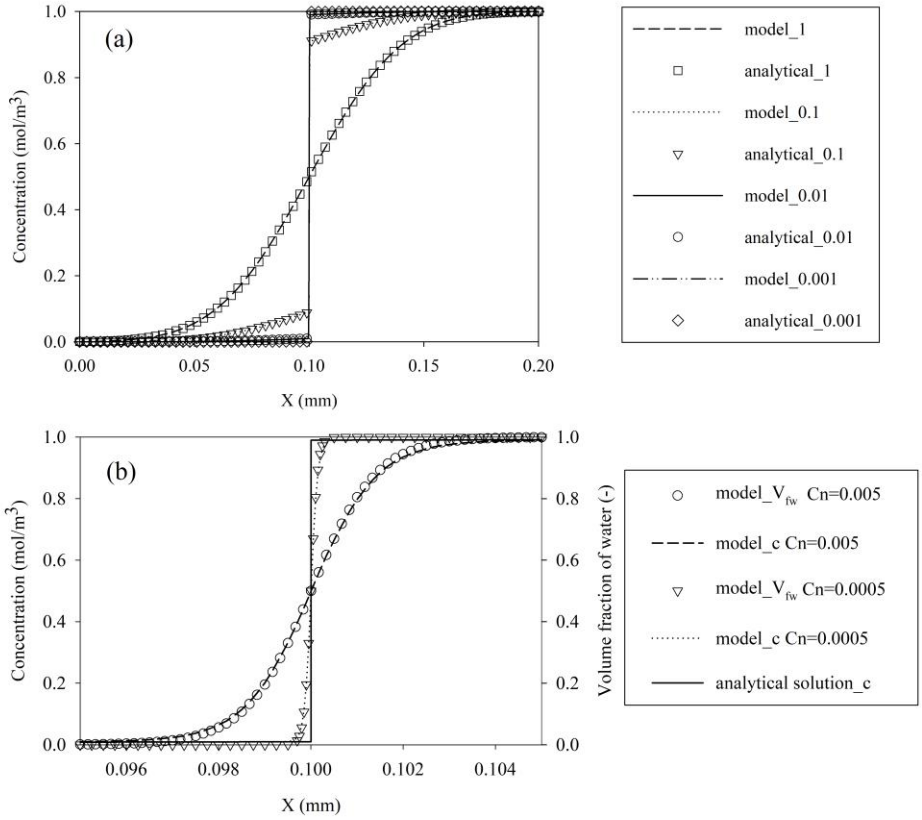

570

571 **Figure 4** Comparison of breakthrough curves of 2-NSA concentration computed
572 analytically and numerically: (a) (at $Cn=5\times10^{-4}$) for the transient mass transfer at
573 t=0.5s, for $P_{ow}=1$, $P_{ow}=0.1$, $P_{ow}=0.01$ and $P_{ow}=0.001$, (b) (at $Cn=5\times10^{-4}$ and $Cn=5\times10^{-3}$) for mass transfer at t=0.5s near the interface region.

575

576 4.1.2 Interfacial reaction and diffusion

577 **Figure 5** shows the results of the reaction-diffusion process at *t*=0.2s, 1s and 2s. The
578 integral of the concentration curves over x (area under the curves) indicates the
579 produced 2-NSA mass in the domain, which is increasing with time. Meanwhile, the
580 produced 2-NSA diffuses from the interface towards the bulk solution following the
581 concentration gradient. The modelling results fit very well the analytical solution,
582 demonstrating that the reaction-diffusion process can be successfully simulated by our
583 modelling approach. **Figure 5** also shows that the mass transfer across the interface is
584 negligible, which indicates that a partitioning coefficient of 0.01 is small enough to
585 describe that the highly water-soluble product 2-NSA remains in the water phase
586 (wetting phase).

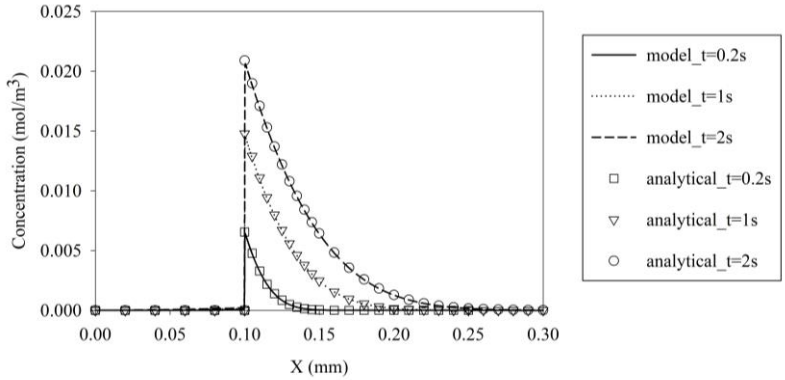

587

588 **Figure 5** Comparison between breakthrough curves of analytical and numerical
589 model simulations (ε=1×10-7m) of the reaction-diffusion process at t=0.2s, t=1s and
590 t=2s.

591

592 **4.2 Model test in a capillary tube**

593 The wettability of the solid wall of the pore space is characterized with the contact
594 angle, which is expressed by Eq.(14) in the model. The contact angle on the solid wall
595 is accurately calculated by the two phase flow model, as shown in **Figure 6**(a) for the
596 setting of θ_w= 45°. Additionally, the characteristic mobility χ, which determines the
597 time scale of Cahn-Hilliard diffusion (Eq.(8)), needs to be chosen pragmatically (Yue
598 et al. 2006). Straining flows can thin or thicken an interface, which must be resisted
599 by large enough Cahn-Hilliard diffusion (Jacqmin 1999). The channel flow here is
600 mainly dominated by capillary forces (*Pe*=5e-4), and there should be no changes in
601 interface configuration during the flow process. It is found when χ is increased by two
602 orders of magnitudes compared to the value of inflow velocity, the thickness and
603 configuration of the interface is ensured to be invariant during the drainage process.

604

605 **Figure 6**(b) shows the concentration profiles for *Pe*=1, *Pe*=10 and *Pe*=100 at *t*=0.04s.
606 The difference in the concentration profiles result from the competition between
607 advection and diffusion. At *Pe*=1, the transfer process is dominated by molecular
608 diffusion, which is verified with model result that the concentration contour lines are
609 almost straight and vertical to the inflow direction. For the Péclet number being
610 *Pe*=10, advection starts to have an obvious effect and concentration contour lines
611 begin to blend. For *Pe*=100, the transfer process is dominated by advection, the solute
612 mass produced at the interface shows a trend to concentrating at the center of the
613 channel. For a stable laminar flow condition in the channel, flow at the center of the
614 channel is faster than the regions near the solid walls, where a no-slip boundary is
615 considered, and all streamlines are parallel to each other. When a two-phase system is
616 considered, near the fluid-fluid interface, the receding phase tends to flowing
617 gathering at the center of the channel flow to restore the stable flow condition, as
618 shown by streamline plot in **Figure 6**(b). Thus, as the effect of the advection, the
619 water-based solute also shows a trend to concentrate at the center of the channel. A
620 similar observation is found in the simulation results from the study for segmented
621 channel two–phase flow by (Yang et al. 2017). The same advection effect exists for
622 all three conditions investigated, with different Péclet numbers. The effect becomes

623 stronger when the diffusion is weak. This simulation provides a verification of the
624 new two-phase reactive transport model.

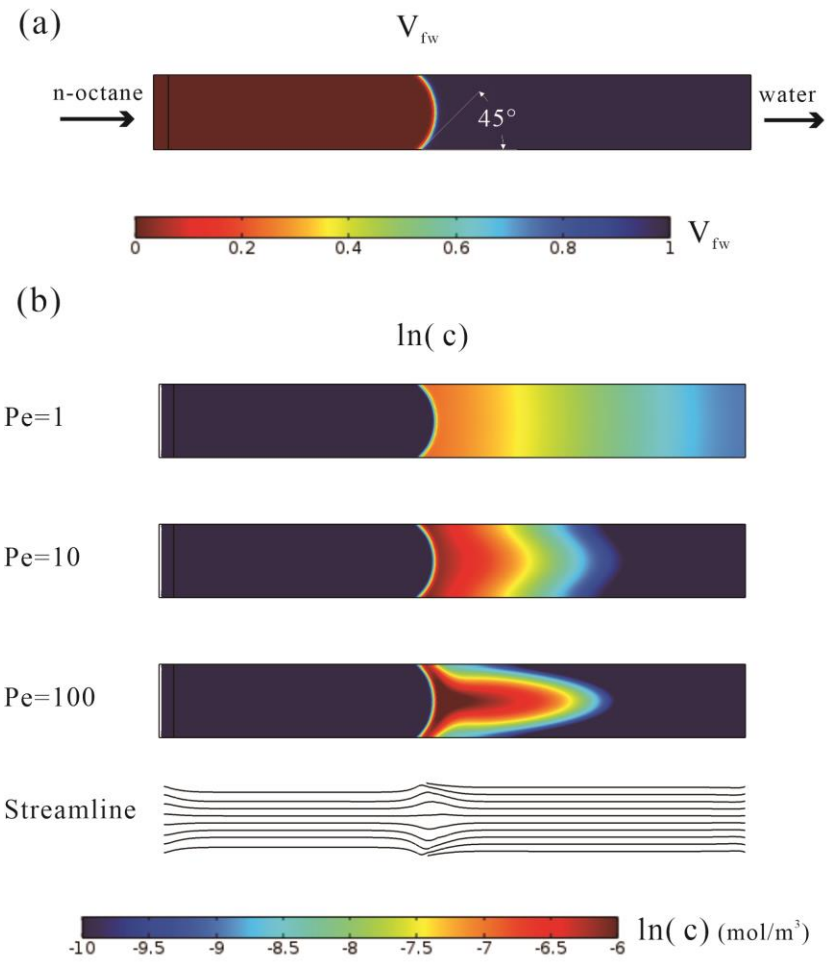

625

626 **Figure 6** Model results of solute transport in octane/water displacement process in a
627 capillary tube: (a) volume fraction of the water phase for with contact angles 45° at
628 t=0.04s (b) Plot of the concentration profiles at the Péclet numbers of *Pe*=1, *Pe*=10
629 and *Pe*=100, as well as the corresponding streamline profile.

630

631 **4.3Application of KIS tracer transport in porous media**

632 We first show the resulting displacement patterns and solute concentration
633 distributions for the four cases in section 4.3.1. The macroscopic parameters are
634 calculated based on the entire domain as shown in section 4.3.2. Then, we distinguish
635 the mobile and immobile zones of the pore space with the velocity in section 4.3.3,
636 and we show the data process to obtain the pattern of the mobile part of the solute
637 mass, which is directly related to outflow based KIS-TT, in section 4.3.4. Finally, we
638 analyze the quantified interfacial area and the solute mass separately in the mobile
639 and immobile zones, in section 4.3.5.

4.3.1. Displacement patterns and solute concentration distribution

Figure 7 shows the distribution of the fluid phases and solute concentration before breakthrough for all four cases. Since the 2-NSA concentration in the immobile water regions near the inlet where the reaction starts early is much larger than that at the moving front, we plot the concentration on a logarithmic scale to better illustrate the distribution of 2-NSA concentration. The fluid phase distribution is shown in **Figure 7**(left). Comparing Case 1 to Case 3, where contact angle is swapped from 45° to 15°, it is observed that the non-wetting phase is more pore-filling for larger contact angles. This is consistent with expectation that less water-wet wall conditions is favorable for drainage. Furthermore, water films are formed on solid walls in the drained pores at θ_w=15°, while at θ_w=45° no water films are observed. The displacement patterns from Basirat et al. (2017) also shows the appearance of the deposited water films at θ_w=15°. Comparing Case 1 to Case 4, the non-wetting phase is more pore-filling when the inflow rate is larger. This means, with a water-wet wall condition of θ_w=45°, a larger capillary number is favorable for the drainage process. This result is in good agreement with Basirat et al. (2017).

The spatial distribution of concentration is shown in **Figure 7**(right). Comparing Case 1 to Case 2, it is observed that the spreading of 2-NSA in these trapped water clusters is much slower during drainage, a direct outcome of the lower diffusivity. Furthermore, for the same Péclet number for Case 1 and Case 3, the concentration values are higher (represented by red color) for case 3, especially in the water films surrounding the solid grains. The formation of water films increases the total interfacial area and leads to a higher production of 2-NSA by hydrolysis. The concentration distribution in Case 4 shows the highest values. This is because, with lower inflow rate, the two fluid phases remain longer in contact with each other until the front reaches the outlet (breakthrough point) which leads to a higher reaction by-product 2-NSA in the water phase.

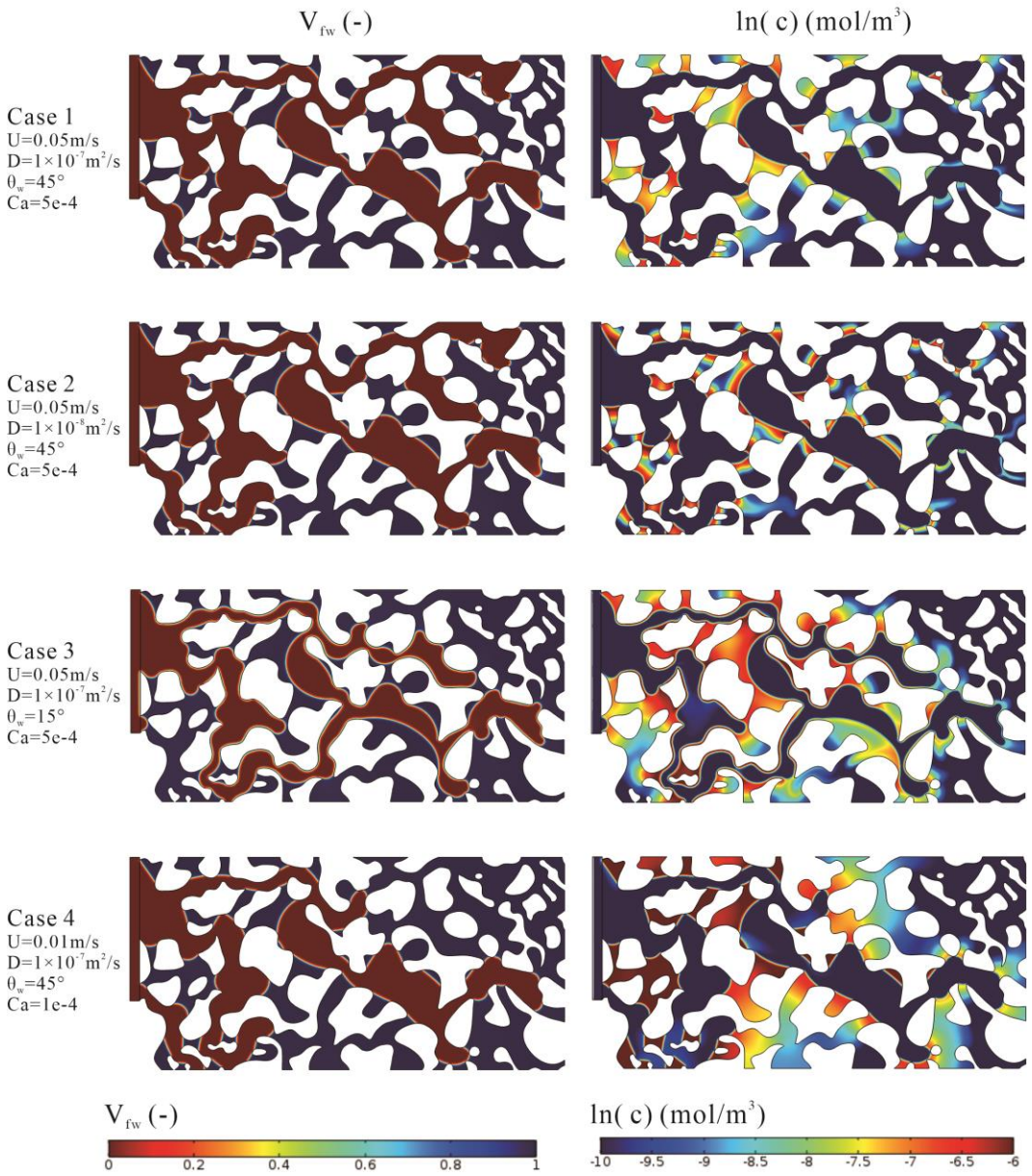

Figure 7 Volume fraction of water phase (left) and solute concentration (right) just before breakthrough for each case.

4.3.2. Derivation of the macroscopic parameters

We analyze the macroscopic parameters on the entire study domain during the drainage process for the four cases as shown in **Figure 8**. Macroscopic parameters for Case 1 and 2 are similar, because they have the same flow parameters and only the diffusivities in these two cases are different. **Figure 8**(a) shows that the non-wetting phase saturation increases linearly with time, which confirms the constant inflow boundary. Case 1 and 2, with a stronger water-wet wall condition and a larger inflow rate, is efficiently drained, leading to a higher saturation at breakthrough. When the non-wetting phase reaches the outlet, S_n starts to decrease, namely the volume of the non-wetting phase in the domain begins to shrink. This is caused by the connected flow-paths of the non-wetting phase between inlet and outlet, formed until time of

683 breakthrough. The non-wetting phase pressure is suddenly decreased leading to the
684 expansion of the wetting phase. This effect was also observed by Basirat et al. (2017).
685 The capillary pressure p_c is defined as the difference between the intrinsic volume
686 averaged pressure of both phases (Ferrari and Lunati 2013), calculated as in Eq.
687 (30)and Eq.(31):

$$p_\alpha = \frac{\int_V p \cdot V_{f,\alpha} dV}{\int_V V_{f,\alpha} dV}, \alpha = w, nw \tag{30}$$

688

$$p_c = p_{nw} - p_w \tag{31}$$

689 where *p* is pressure. The capillary pressure fluctuations in **Figure 8**(b) are caused by
690 Haines jumps, when the oil front moves through the pore neck into a wider pore body
691 during the drainage process (Armstrong et al. 2015). The average capillary pressure
692 for Case 3 is larger than that of Case 1 and 2, which means a larger P_c is needed for
693 more water-wet conditions during drainage with the same inflow rate which agrees
694 with the results of Rokhforouz and Akhlaghi Amiri (2019). The overall capillary
695 pressure is the lowest in Case 4 during the displacement. This is due to that the
696 invading non-wetting phase pressure is smaller at the lower inflow rate, which causes
697 the corresponding calculated p_c by Eq.(30) and Eq.(31) also smaller than other cases.
698 The specific interfacial area (*SIA*) is calculated by Eq.(32):

$$a_{wn} = \frac{A_{wn}^{dif}}{b_{wn}} \cdot \frac{1}{V_p} \tag{32}$$

699 where A_{wn}^{dif} is the interface region within $V_{fw} \in [0.05, 0.95]$, b_{wn}=4.16ε is the thickness
700 of the reaction region obtained from Eq.(6), with the diffusive interface having a
701 width of ε=1e-6m, and V_p is the total volume of the porous media that is studied.
702 **Figure 8**(c) shows that a_{wn} in Case 3 is much larger than that in the other cases, which
703 is due to the formation of deposited water films. The difference is large because the
704 magnitude of the film associated to interfacial area is quite large, as it forms on all
705 solid walls in the drained pores. The specific interfacial area in all cases shows
706 approximately a linear increase with the constant inflow boundary, which is verified
707 with the LBM simulation by Liu et al. (2015) for the process of water displaced by
708 CO_2 in a homogeneous pore network consisted of circular grains. With a known
709 specific interfacial area and saturation, the volume averaged 2-NSA concentration for
710 the domain can be calculated as in Eq.(33):

$$c_t = \frac{\int_{t_0}^{t} A_{wn}^{dif}(t) \cdot R_c^{dif} dt}{V_p \cdot S_w(t)} \tag{33}$$

711 **Figure 8**(d) shows that the solute concentration in the study domain (lines) fit that
712 calculated from Eq.(33) (open circles), consistent with mass conservation, and this
713 proves the model simulates the constant zero-order interfacial reaction accurately.
714 This also means, for macro-scale application of the tracer, when saturation and 2-NSA
715 concentration is measured for a unit volume of the porous media, the specific
716 interfacial area can be calculated, which is confirmed with the theory of the KIS
717 tracer.

718

Nevertheless, the domain-averaged 2-NSA concentration is difficult to be obtained with common measurement techniques in natural porous media. A more applicable way is measuring the 2-NSA concentration at the outflow, such as in the column experiments shown in Tatomir et al. (2018), where the 2-NSA concentrations are measured at the outlet of the column. In this case, the fraction of the 2-NSA mass reacted in the immobile zones is not detected. To quantify these 2-NSA mass carried by the moving water that can be detected, the mobile and immobile zones need to be differentiated.

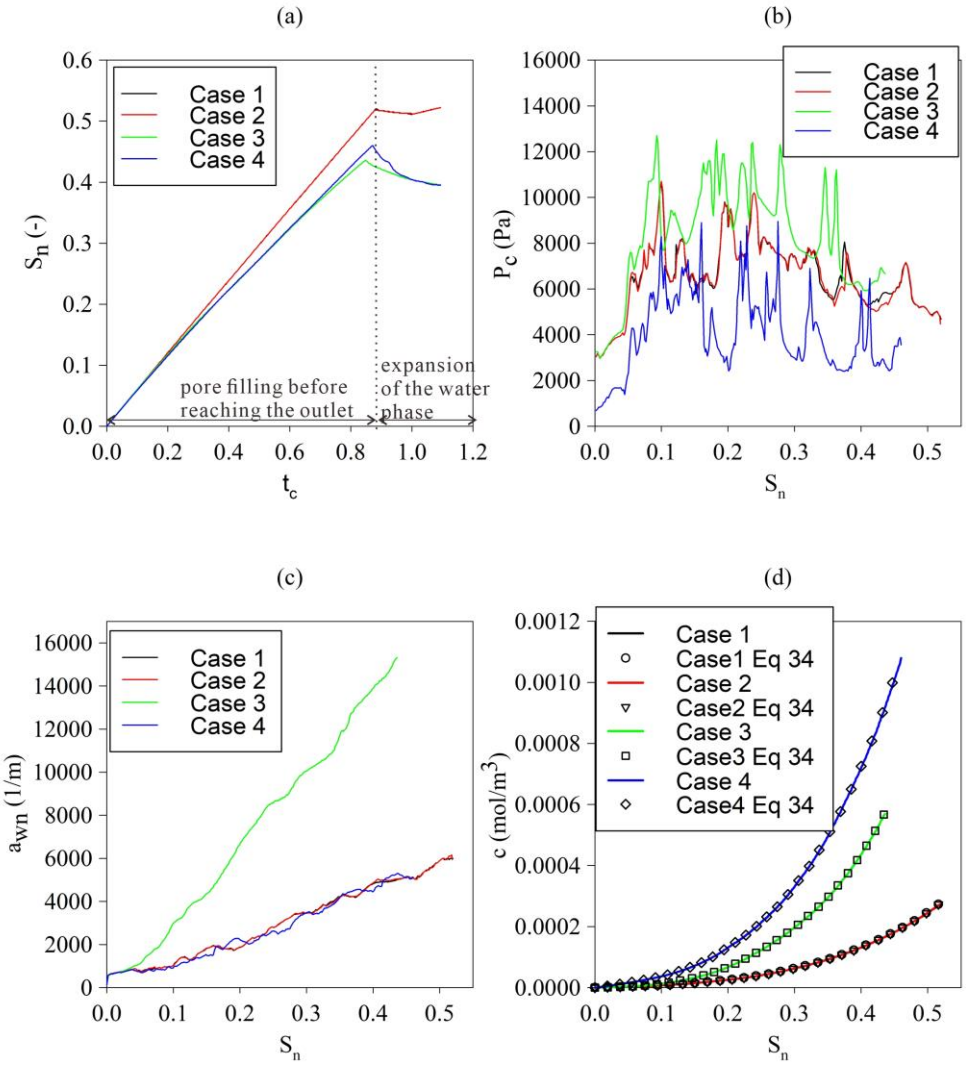

Figure 8 Macro-scale parameters during drainage process for each case. (a) Non-wetting phase saturation versus the characteristic time; (b) Capillary pressure versus the non-wetting saturation; (c)Total specific interfacial area versus the non-wetting saturation; (d) Comparison between the domain average solute concentration plotted versus the non-wetting saturation in lines, and the domain average solute concentration calculated by Eq.(33) with the interfacial area from subfigure c in makers.

736 4.3.3. Identification of the mobile and immobile zones

737 The immobile zones are the regions were flow velocity is low so that mass transport is
738 only diffusion controlled (Karadimitriou et al. 2016). The Péclet number can be
739 calculated as $Pe_{local} = u * L_c/D$, where **u** is the velocity field, L_c is the characteristic
740 length equal to the average throat width L_c=8μm (Rokhforouz and Akhlaghi Amiri
741 2019), and D is diffusivity. The mobile zones are generally defined as zones with
742 Pe>>1 (Smedt and Wierenga 1984; Chhabra and Shankar 2018). The threshold Péclet
743 numbers and corresponding velocity values for the four cases are chosen such that
744 capillary trapped zones and dead-end pores can be distinguished. **Figure 9** shows an
745 example for Case 1 at the beginning of the drainage: the region with Pe<5 is classified
746 as the immobile zone, and the rest parts are mobile zones. It is observed from **Figure**
747 **9** that the stagnant zones are clearly classified in dark color.

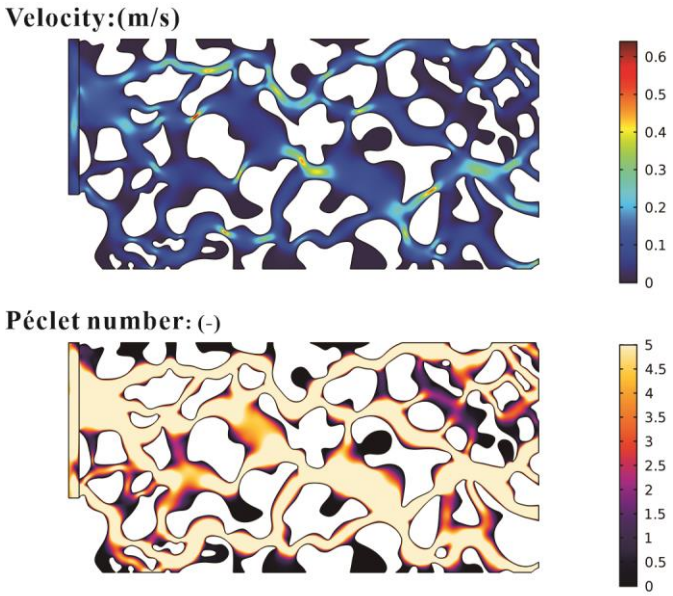

748

749 **Figure 9** Plot of the velocity and local Péclet numbers to distinguish mobile and
750 immobile zones at the beginning of the drainage process.

751

752 4.3.4. Patterns of interface and solute concentration for mobile and immobile zones

753 We take the drainage process in Case 1 as an example. We plot the 2-NSA
754 concentration in **Figure 10**(a), where the n-octane phase with negligible 2-NSA
755 concentration is plotted in grey. The corresponding velocity field is plotted in **Figure**
756 **10**(b), where mobile and immobile zones are separated by employing the above
757 threshold Péclet number. Comparing **Figure 10**(b) with **Figure 9**, it can be observed
758 that the immobile zones are expanded obviously during the displacement process. At
759 the beginning of drainage, the porous medium is only filled with water, meaning a
760 single phase flow condition, and the immobile zones are only found in dead-end
761 pores. With displacement going, the capillary trapped water is keeping formed, which
762 causes the expansion of the immobile zones. At the end of the drainage process (the
763 system becoming steady state), several flow channels turn into immobile zones. Only
764 that channel, through which the front first reached the outlet, keeps flowing
765 continuously with the invading phase. Looking both the concentration profiles in
766 **Figure 10**(a) and the velocity in **Figure 10**(b), we observe that the transported

767 concentration pattern in the mobile zones and immobile zones are different. In the
768 immobile zones, the produced 2-NSA spreads in the vicinity of the interface to lower
769 concentration regions inside the trapped water clusters, and this process is diffusion-
770 driven. In the mobile zones the 2-NSA spreads much faster than in the immobile
771 zones, along with the formation of long 2-NSA plumes. This fast spreading is
772 dominated by advection at the moving front, related to macro-scale dispersion. After
773 filtering with the threshold Péclet number the 2-NSA concentration profile is plotted
774 in **Figure 10**(c), where only the 2-NSA located in the mobile zone is left and the
775 immobile zones are depicted in black. With the concentration map of the 2-NSA in
776 the mobile zones during the displacement (**Figure 10**c), it is clear that the 2-NSA
777 carried by the moving water is produced and located on the menisci at the moving
778 front in the main flow channels. And the moving water at front is not connected to the
779 dispersed water clusters trapped in dead-end pores or throats, which means there is no
780 2-NSA mass exchange between them. This part of 2-NSA mass in the mobile zones is
781 vital for the outflow based KIS tracer test.

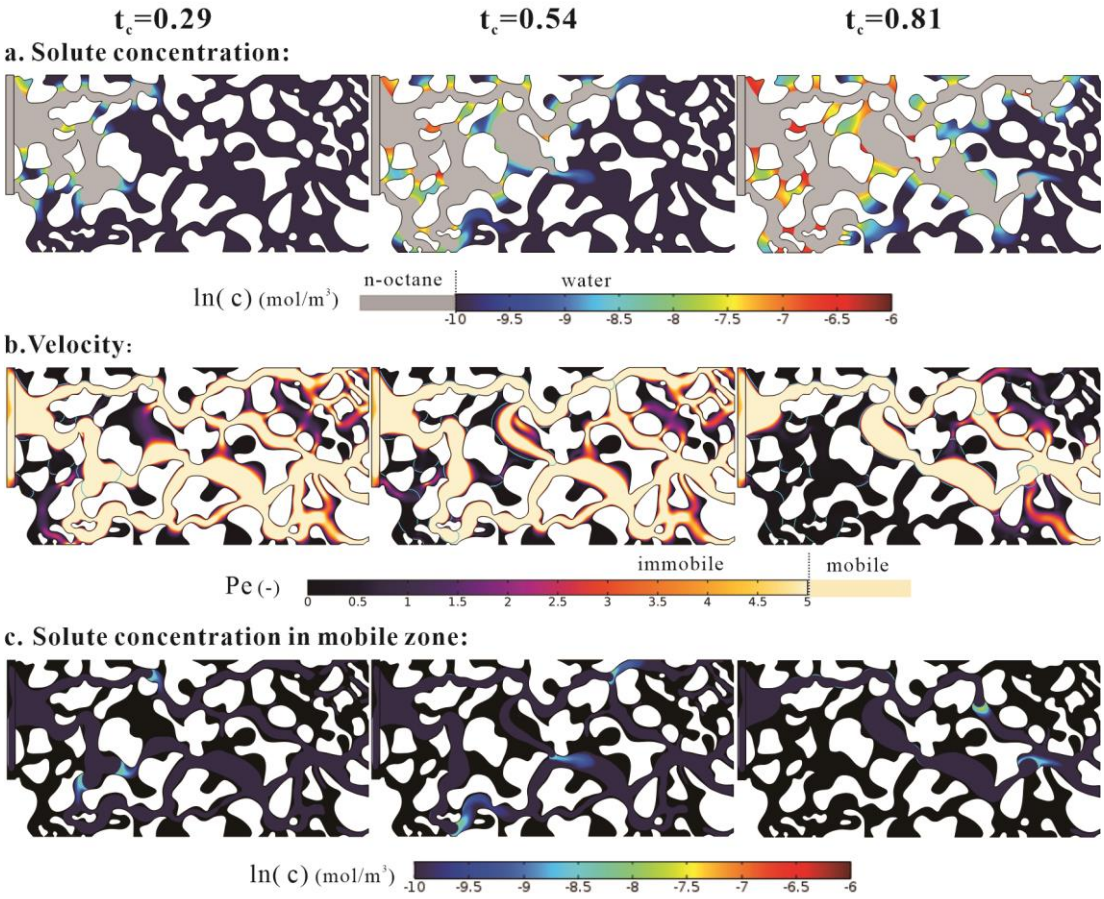

782

783 **Figure 10** Plot of the process to distinguish the mobile and immobile zones and
784 corresponding mobile and immobile interfaces and solute mass for Case 1. (a): 2-NSA
785 concentration (with n-octane phase in gray colour); (b): mobile and immobile zones
786 separated with a threshold velocity (0.06m/s), with interface in Cyan; (c):
787 concentration of 2-NSA in the mobile zones, with the immobile zones filtered by the
788 threshold velocity in black.

789

790 4.3.5. Interpretation and implications of the tracer concentration

791 Mobile and immobile SIA are plotted in **Figure 11** for changes in saturations during
792 drainage. The mobile *SIA* values range between 200 – 1300 1/m (**Figure 11**a) while
793 the immobile *SIA* can reach an order of magnitude higher up to 15000 1/m (**Figure**
794 **11**b). The mobile SIA has strong oscillations during drainage, which is mainly caused
795 by switching of the mobile and immobile interfaces at the front. When one meniscus
796 at the front meets narrow pore necks, the fluid will become stagnant for several time
797 steps, during which the meniscus that originally counted as the mobile interface will
798 becomes temporarily immobile. Meanwhile, the nearby menisci, which are originally
799 immobile, can also become mobile due to the equilibrium of the local pressure. As the
800 menisci have different sizes, this switching of the mobile and immobile interfaces
801 causes the oscillations of the curve of the accounted mobile interfacial area during the
802 displacement. The overall change in mobile SIA is relatively small during drainage,
803 and its values are similar for all four cases. This can be attributed to the fact that the
804 mobile interfacial area results from the menisci at the moving front, which depend on
805 the width and geometry of the flow channels. On the other hand, the immobile *SIA*
806 increases approximately linearly with saturation during the displacement process, due
807 to the formation of trapped water clusters and films. For the immobile interfacial area,
808 Case 3 shows the largest SIA due to the formation of water films.

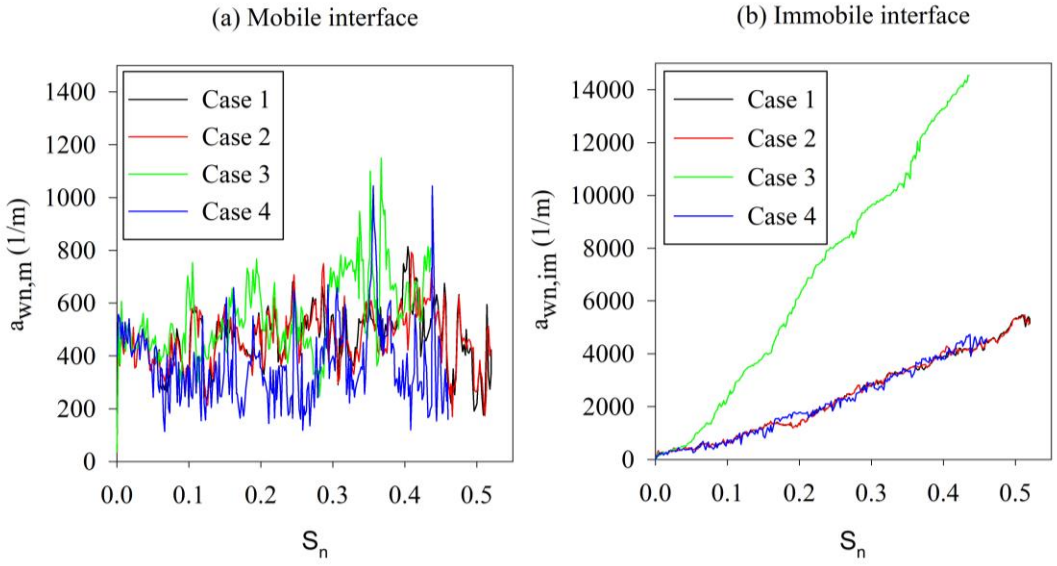

809

810 **Figure 11** Mobile and immobile specific interfacial areas during the drainage process
811 for the four cases.

812

813 Furthermore, the temporal change in total 2-NSA mass in the mobile zones (M^m) and
814 immobile zones (M^{im}) is shown in **Figure 12**, where the mobile 2-NSA mass is
815 quantified as the sum of the 2-NSA mass in the mobile zone, and in the part exiting
816 the domain through the outlet. It is found that the 2-NSA mass in the mobile zones is
817 much smaller than that in the immobile zones. The curve oscillations for the
818 quantified solute mass in **Figure 12** are also caused by the switching of the mobile
819 and immobile zones during the Haines Jumps.

820

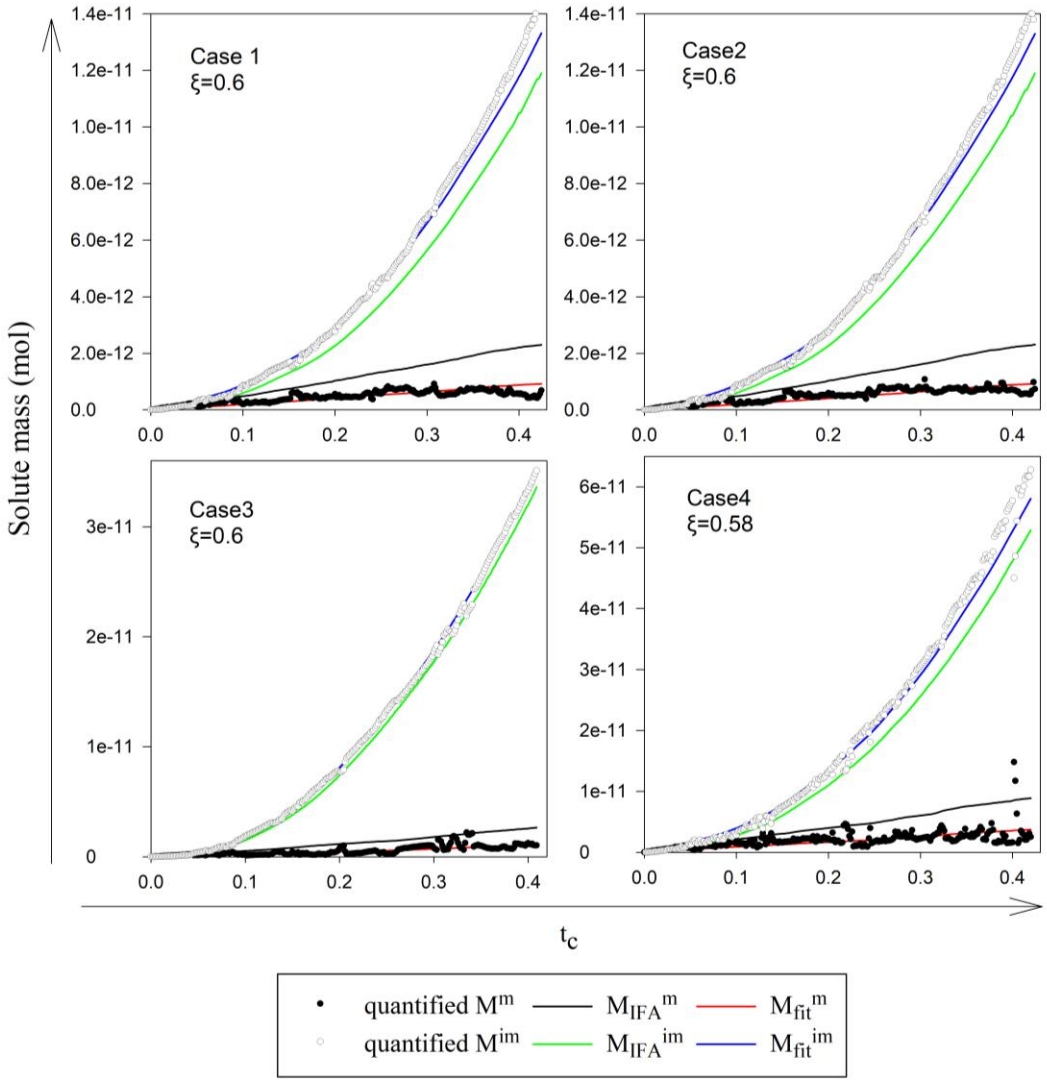

821

822 **Figure 12** Plot of 2-NSA mass (*M*) in the moving water phase and in immobile zones
823 for each case, and the 2-NSA mass produced by mobile and immobile interface (M_{IFA})
824 calculated from Eq.(34), as well as the 2-NSA mass (M_{fit}) curve calculated from
825 Eq.(35)(36)(case1: ξ=0.6, case2: ξ=0.6, case3: ξ=0.6, case4: ξ=0.58).

826

827 We investigate if the 2-NSA mass transported by the mobile water phase can be
828 related to the mobile interfacial area. Knowing the mobile and immobile interfacial
829 areas, we can calculate the 2-NSA mass M_{IFA} produced by them respectively by
830 Eq.(34).

$$M_{IFA}^{m,im}(t) = \int_{t_0}^{t} A_{wn}^{m,im}(t) \cdot R_c^{dif}\, dt \tag{34}$$

831 where superscripts m and im, indicate mobile and immobile, respectively. For the
832 mobile zones, we found both curves of M^m and $M_{IFA}{}^m$ show (roughly) a linear increase
833 with dimensionless time, but the curve of $M_{IFA}{}^m$ has a larger slope than M^m. This
834 means a constant fraction of the 2-NSA produced by the mobile interface becomes
835 residually trapped in the immobile zones. For the immobile zones, the curve of both

836 M^{im} and $M_{IFA}{}^{im}$ show a parabolic increase, and the curves show that M^{im} is larger than
837 $M_{IFA}{}^{im}$. Because the total 2-NSA mass matches that calculated from the total
838 interfacial area (**Figure 8**(d)), the additional fraction of immobile 2-NSA mass is
839 derived from the retention of part of 2-NSA mass produced at the mobile interface.
840 We introduced a residual fraction ξ in Eq.(34) to formulate the relationship between
841 mobile interface and 2-NSA in moving water, as well as immobile interface with 2-
842 NSA mass in immobile zones as Eq.(35) and Eq.(36):

$$M_{fit}^{m}(t) = \int_{t_0}^{t} [A_{wn}^{m}(t) \cdot (1 - \xi)] \cdot R_c^{dif} dt \tag{35}$$

843

$$M_{fit}^{im}(t) = \int_{t_0}^{t} [A_{wn}^{im}(t) + \xi A_{wn}^{m}(t)] \cdot R_c^{dif} dt \tag{36}$$

844 where M_{fit} is the 2-NSA mass calculated by adding the residual fraction. The curves
845 are better fitted by adding the residual fraction as shown in**Figure 12**. The deviation
846 of the curves from M and M_{fit} is only found near the end of the drainage process,
847 because a large decrease in the mobile zones occurs shortly before breakthrough.

848

849 The residual fractions determined for the four studied cases have similar values
850 ranging from 0.58 to 0.6. A zoom-in region for the retention process is shown in
851 **Figure 13**. The retention of the reacted solute in the moving water (at the front)
852 occurred when the mobile interface at the moving front splits and forms new
853 interfaces in the immobile zones, including dead-end pores and capillary trapped
854 zones. During this process, a part of the 2-NSA carried by the mobile interface is
855 transported by advection into these newly formed immobile zones. The retention
856 process happens with the formation of the immobile interface during the displacement,
857 leading to an approximate constant residual fraction in the relationships of Eq.(35)
858 and Eq.(36).

859

860 The results imply that when the 2-NSA concentration in the outflow is measured and
861 the residual fraction is known, the mobile interfacial area during the drainage can be
862 measured with the KIS-TT.

863

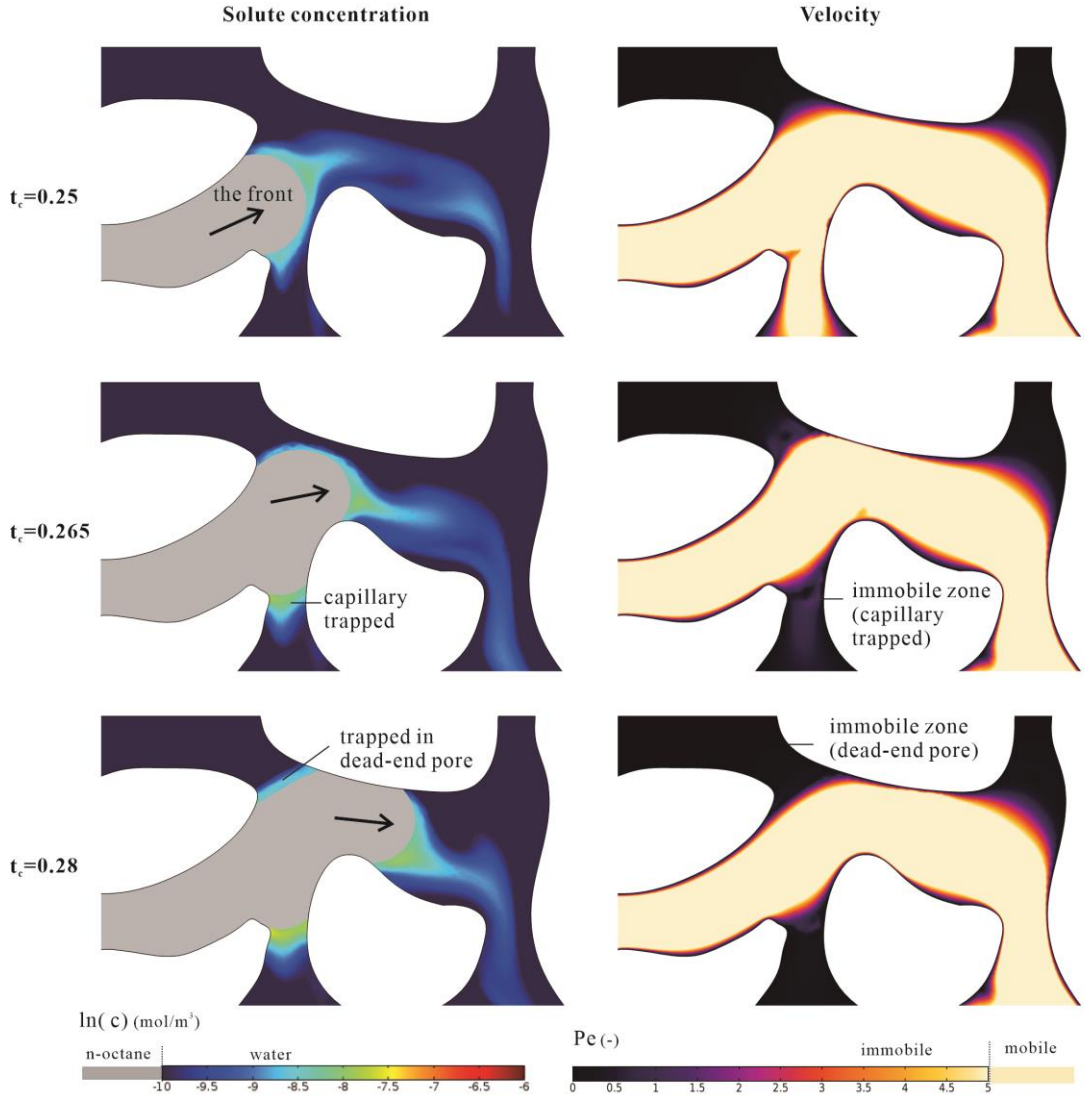

Figure 13 Retention process of 2-NSA produced at the mobile interface into the immobile zones, in a zoom-in region from Case 1 at t_c=0.25, t_c=0.265 and t_c=0.28. The left diagrams show the spatial distribution of solute concentrations in main flow direction of the front in black arrow for different times with the corresponding spatial velocity field on the right.

5. Summary and Conclusions

We proposed and demonstrated a novel pore-scale model for simulating the KIS tracer reactive transport process for two-phase flow conditions in a porous medium. In the mathematical model, a continuous species transport formula consistent with PFM was derived. One major advantage of the model is that the fluid-fluid interface hydrolysis reaction of the KIS tracer, which is approximated by a zero-order reaction, can be directly implemented in the diffusive interface approach. We first provide two types of verifications of the model. By comparing the solute concentration and water volume fraction across the interface in a simple diffusion process, we showed that the solute concentration at the diffusive interface can be accurately calculated by the model. We found that for low partitioning coefficients (P_{ow}=0.01), the model

adequately describes the selective distribution of 2-NSA into water. Additionally, the simultaneous process of 2-NSA interfacial reaction and diffusion was verified by comparing the numerical results and the analytical solution of the reaction-diffusion equation. Next, the model was tested by simulating the drainage process (i.e., wetting phase displacement by the non-wetting phase) in a capillary tube. After testing the solute transport model for different Péclet numbers, we found that the concentration profile changes are diffusion-dominated at Pe=1 and advection-dominated at Pe=100.

Finally, the model was applied to a realistic 2D porous medium. Four cases with different diffusivities, contact angles and inflow velocities were simulated and the corresponding macro-scale parameters (saturation, capillary pressure, interfacial area and 2-NSA concentration) were obtained from the pore-scale results. By comparing the four cases it could be shown that a larger contact angle and a larger inflow rate lead to larger non-wetting phase saturations. The overall capillary pressure during drainage was larger for smaller contact angles and larger inflow rates. The specific interfacial area in the case where there are deposited water films is much larger than without the films. We calculated the average macro-scale 2-NSA concentration from the pore-scale determined fluid-fluid interfacial areas. The averaged 2-NSA concentration measured in the domain fitted that calculated from the interfacial area, providing a verification for the reactive transport model.

To understand how immobile zones affects the detectable solute mass in the outflow-based measurements, we quantified the interfacial area and the reacted 2-NSA mass separately in the mobile and immobile zones. It was observed that the fraction of 2-NSA mass transported by the moving water is related to the mobile interface. It was found that the mobile *SIA* is much lower than the total SIA (ca. 10%) and it varies little during the drainage process. We propose an interpolation relationship between the 2-NSA mass in the mobile zones and the mobile interfacial area. The relationship is formulated by adding a residual factor. This term relates to the part of 2-NSA produced by mobile interface that becomes residual in the immobile zones.

This study showed that the mobile interface, or the moving interface, plays an important role for the transport of the receding phase based interfacial reacted solute in the displacement process. The KIS-TT, which is capable of measuring the mobile interface, can be a valuable technique in understanding the coupled flow and reactive transport processes in dynamic two-phase flow systems. Future work is required to study if the residual fraction varies when applied to different pore geometries, or when using different fluid -porous media systems with wider ranges of wettability and flow rates. Future work is also required to improve our macroscopic model of KIS tracer reactive transport (Tatomir et al. 2015, 2018), for further including the different transport patterns in the mobile and immobile zones observed at the pore-scale.

Acknowledgement

We thank Tobias Licha for the constructive dialogue about the KIS tracer and overall support of the work. We thank Rainer Helmig and Holger Class (from the SFB1313

Collaborative Research Center) for the support in conducting and further extending this work.

We acknowledge DFG Project 428614366, European Community's 7th Framework Programme FP7 under grant number 309067 (trust-co2.org), and Horizon 2020 Research and Innovation Programme (https://ec.europa.eu/inea/en/horizon-2020/projects/H2020-Energy/Shale-gas/FracRisk) under grant number 636811.

HS acknowledges funding by the Deutsche Forschungsgemeinschaft (DFG, German Research Foundation) under Germany's Excellence Strategy - EXC 2075 - 390740016. All data used to support this work are reported in the manuscript and the Appendix in the respective tables and figures.

Appendix A validation of the phase field method

Appendix A shows the validation of modeling two-phase flow with the phase field method, through a pressure gradient driven two-phase channel flow (Appendix A1), a deformed bubble retraction process driven by the surface tension (Appendix A2), as well as benchmark of the calculated deposited film thickness for a quick displacement process (Appendix A3).

A1 Viscous coupling co-current flow

The two-phase flow model is validated through simulating a channel co-current flow, where water phase flow along channel walls and oil phase flow in the centre as shown in **Figure 14**(a). The inlet boundary and the outlet boundary are constant pressure (P_{in}=0.1pa and P_{out}=0). The channel wall is no-slip, and initially zero flow velocity in domain. Both phases occupy half width of the half-channel 0.1mm. The channel is long enough to reduce any boundary effects. Due to continuous flow of both phases, the effect of surface tension is small. This simulation mainly tests if the pressure and viscous forces are work well in the model by comparing to the one dimensional analytical solution of Navier-Stokes equation in channel with width l (Eq.(37), Eq.(38)) (Yiotis et al. 2007).

At $0.5l < x < l$

$$u(x) = \frac{\nabla p}{2\mu_w}(l^2 - x^2) \tag{37}$$

At $0 < x < 0.5l$

$$u(x) = \frac{3l^2 \cdot \nabla p}{8\mu_w} + \frac{\nabla p}{2\mu_n}\left(\frac{l^2}{4} - x^2\right) \tag{38}$$

After a transient period at beginning, the model reaches steady state and the velocity remains constant. **Figure 14**(b) plot the velocity profile along the channel width for viscosity ratio (oil to water) β=10 and β=0.1. Mixture of viscosity of both fluids at interface causes derivation when interface is thick, thus thinner interface provides more accurate modeling result, which needs to be supported by adequately fine mesh. The model result shows good consistency with analytical solution at Cn=0.005, h=0.5ε.

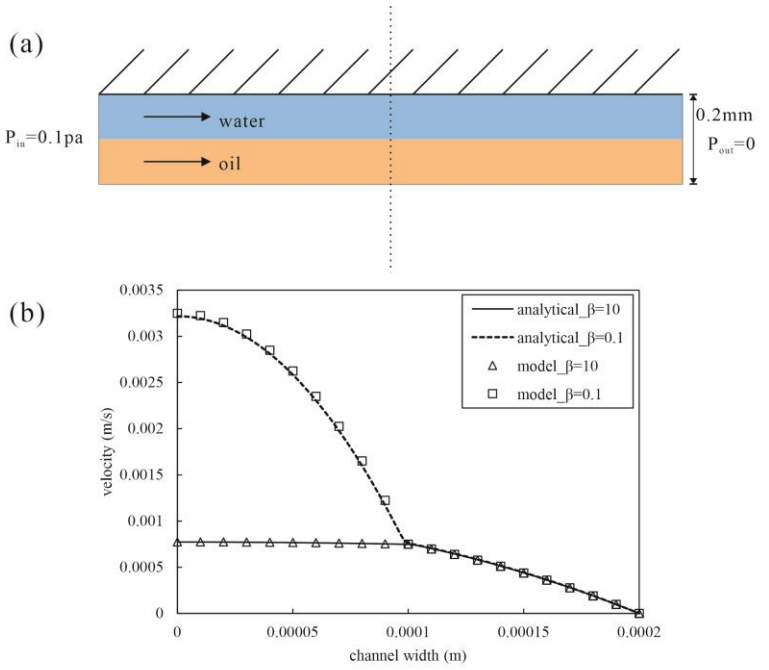

Figure 14 Validation with channel co-current two phase flow (a) Sketch of viscous coupling channel co-current flow. (b) Comparison of velocity profile along the channel width from the model and the analytical solution at β=10 and β=0.1.

A2 Bubble relaxation

Bubble relaxation is experimental well studied problem, which provides a good benchmark for the two-phase flow model. During retraction of an initially elliptic bubble towards the sphere in a quiescent matrix, the major and minor axis is measured for back calculation the surface tension between two fluids. Parameters used here are according to experiment by Guido and Villone (1999). The dispersed phase has density of 965 kg/m3 and viscosity μ_d=109 Pa*s and the continuous phase has density of 920 kg/m^3 and viscosity μ_c=81 Pa*s. Viscous fluids are used in these experiments to avoid effect of inertia. Interfacial tension σ=2.58 mN/m. Radius of the bubble at rest R_0=55μm. Bubble is located at center of a square domain with side length $4R_0$. The deformation parameter D=(a-b)/(a+b), where, a and b are major axis and minor axis respectively. Time is scaled with capillary time $t_c=\mu_c R_0/\sigma$. Two bubble retraction experiments is simulated with initial bubble deformation of D_0=0.22 and D_0=0.42 (**Figure 15**a). **Figure 15**(b) Plot the resulting data ln(D/D_0) verses the capillary time. For sake of comparison, following Guido (1999), the original of the abscissa is taken corresponding to a value of D called D_0' (D_0'=0.13 for D_0=0.22 and D_0'=0.1 for D_0=0.42). The results are further compared to the theoretical approach by (Rallison 1984) in limit of small deformations (Eq.(39)).

$$D = D_0 exp(-\frac{40(\beta+1)}{(2\beta+3)\cdot(19\beta+16)}\cdot t_c) \tag{39}$$

Where β is the viscosity contract $\beta=\mu_d/\mu_c$. When surface tension is fixed, the surface energy density depends on the interface thickness, which determined the retraction process. With interface thickness Cn=0.02 (mesh size h=0.4ε, mobility χ=1), the numerical results fit the experimental results, which all falls on the same master curve

992 that represented by Eq.(39). Derivations of numerical and experimental results from
993 theoretical approach only observed when deformation of bubble is quite large (Guido
994 and Villone 1999).

995

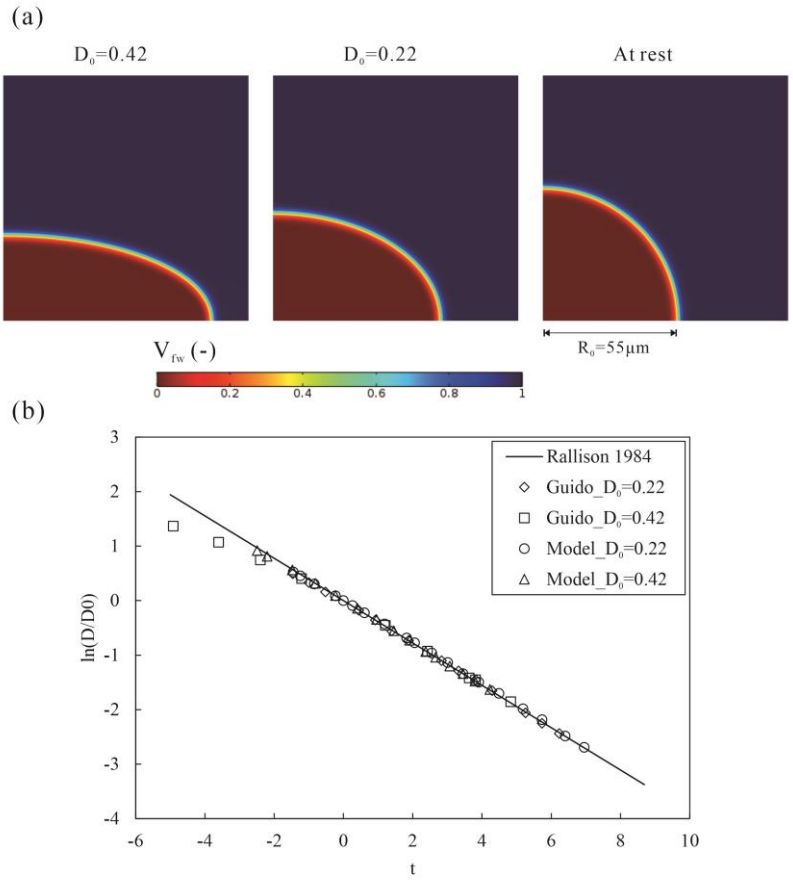

996

997 **Figure 15** Validation with bubble retraction process (a) Plot of simulated bubble at
998 beginning with deformation of D_0=0.22 and D_0=0.42, and at the end that bubble at
999 rest (b) Comparison of ln(D/D_0) from modeling results to experimental and theoretical
1000 results.

1001

1002 **A3 Deposited film thickness**

1003 For the two phase flow in porous media, the wetting phase may form thin films on the
1004 grain surface during a displacement process (Brusseau et al. 2009; Brusseau et al.
1005 2010; McDonald et al. 2016b). To accurately capture these films, we consider a quick
1006 displacement process of ethanol ($\rho_{ethanol}$=789kg/m^3 and $\mu_{ethanol}$=1.2mPas) with air
1007 (ρ_{air}=1kg/m^3 and μ_{air}=18μPas) in a capillary tube according to the experiment
1008 demonstrated by Aussillous and Quéré (2000), for the model benchmark. The
1009 interfacial tension for ethanol/air σ=0.02 N/m. The tube is 0.8mm long with a radius
1010 of R=0.05mm, and both side boundaries are solid wall. The tube is initially filled
1011 with ethanol and air is injected from the left side with U_{in}=0.4m/s at t=0. A sketch of
1012 the model setup is shown in **Figure 16**(a). Aussillous and Quéré (2000) proposed the
1013 thickness of the deposited film on the wall, which is given by the semi-empirical
1014 Taylor's law (Eq.(40)):

$$\frac{m}{R} = \frac{1.34Ca^{2/3}}{1 + 3.35Ca^{2/3}} \tag{40}$$

where m is the film thickness, Ca is the capillary number: $Ca = u * \mu_l/\sigma$, and m=4.36μm is obtained from the formula. In the model, the mesh size near the wall boundary is refined to h=1μm to better resolve the deposit film, and the mesh size in middle of the tube h=2μm. The results of the drained tube at t=1ms are shown in **Figure 16**(b), and the film thickness is obtained as 4.42μm, which has a relative error of 1.3% compare to Taylor's law.

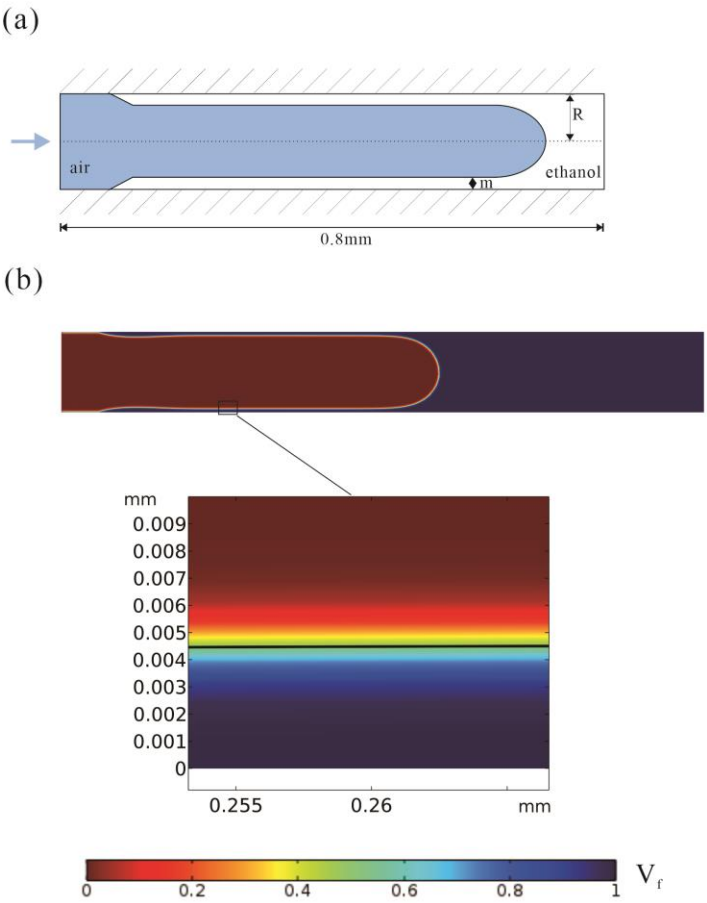

Figure 16 Benchmark of simulated film thickness (a quick displacement process of ethanol with air in a capillary tube): (a) Sketch of the model setup(b) volume fraction of ethanol at t=1ms. The zoom-in frames show the deposited film thickness (solid black line is the center line of the diffuse interface V_f=0.5).

Reference

Akhlaghi Amiri HA, Hamouda AA (2013) Evaluation of level set and phase field methods in modeling two phase flow with viscosity contrast through dual-permeability porous medium. Int J Multiph Flow 52:22–34 . https://doi.org/10.1016/j.ijmultiphaseflow.2012.12.006

Akhlaghi Amiri HA, Hamouda AA (2014) Pore-scale modeling of non-isothermal two phase flow in 2D porous media: Influences of viscosity, capillarity,

1034 wettability and heterogeneity. Int J Multiph Flow 61:14–27 .
1035 https://doi.org/10.1016/j.ijmultiphaseflow.2014.01.001

1036 Alpak FO, Riviere B, Frank F (2016) A phase-field method for the direct simulation
1037 of two-phase flows in pore-scale media using a non-equilibrium wetting
1038 boundary condition. Comput Geosci 20:881–908 .
1039 https://doi.org/10.1007/s10596-015-9551-2

1040 Armstrong RT, Evseev N, Koroteev D, Berg S (2015) Modeling the velocity field
1041 during Haines jumps in porous media. Adv Water Resour 77:57–68 .
1042 https://doi.org/10.1016/j.advwatres.2015.01.008

1043 Aussillous P, Quéré D (2000) Quick deposition of a fluid on the wall of a tube. Phys
1044 Fluids 12:2367–2371 . https://doi.org/10.1063/1.1289396

1045 Basirat F, Yang Z, Niemi A (2017) Pore-scale modeling of wettability effects on
1046 CO2–brine displacement during geological storage. Adv Water Resour
1047 109:181–195 . https://doi.org/10.1016/j.advwatres.2017.09.004

1048 Bird RB (2002) Transport phenomena. Appl Mech Rev 55:R1–R4 .
1049 https://doi.org/10.1115/1.1424298

1050 Blunt M, King P (1990) Macroscopic parameters from simulations of pore scale flow.
1051 Phys Rev A 42:4780–4787 . https://doi.org/10.1103/PhysRevA.42.4780

1052 Bond WJ, Wierenga PJ (1990) Immobile water during solute transport in unsaturated
1053 sand columns. Water Resour Res 26:2475–2481 .
1054 https://doi.org/10.1029/WR026i010p02475

1055 Bromly M, Hinz C (2004) Non-Fickian transport in homogeneous unsaturated
1056 repacked sand. Water Resour Res 40: .
1057 https://doi.org/10.1029/2003WR002579

1058 Brusseau ML, Narter M, Janousek H (2010) Interfacial Partitioning Tracer Test
1059 Measurements of Organic-Liquid/Water Interfacial Areas: Application to Soils
1060 and the Influence of Surface Roughness. Environ Sci Technol 44:7596–7600 .
1061 https://doi.org/10.1021/es101312n

1062 Brusseau ML, Narter M, Schnaar G, Marble J (2009) Measurement and Estimation of
1063 Organic-Liquid/Water Interfacial Areas for Several Natural Porous Media.
1064 Environ Sci Technol 43:3619–3625 . https://doi.org/10.1021/es8020827

1065 Cahn JW, Hilliard JE (1959) Free Energy of a Nonuniform System. III. Nucleation in
1066 a Two-Component Incompressible Fluid. J Chem Phys 31:688–699 .
1067 https://doi.org/10.1063/1.1730447

1068 Carslaw HS, Jaeger JC (1959) Conduction of heat in solids

1069 Chen L, Wang M, Kang Q, Tao W (2018) Pore scale study of multiphase
1070 multicomponent reactive transport during CO2 dissolution trapping. Adv
1071 Water Resour 116:208–218 . https://doi.org/10.1016/j.advwatres.2018.02.018

1072 Chhabra R, Shankar V (eds) (2018) Chapter 6 - Transport Processes in Microfluidic
1073 Applications. In: Coulson and Richardson's Chemical Engineering (Seventh
1074 Edition). Butterworth-Heinemann, pp 529–546

1075 Culligan KA, Wildenschild D, Christensen BSB, Gray WG, Rivers ML, Tompson
1076 AFB (2004) Interfacial area measurements for unsaturated flow through a
1077 porous medium. Water Resour Res 40:W12413 .
1078 https://doi.org/10.1029/2004WR003278

1079 Dalla E, Hilpert M, Miller CT (2002) Computation of the interfacial area for two-fluid
1080 porous medium systems. J Contam Hydrol 56:25–48

1081 Ding H, Spelt PDM (2007) Wetting condition in diffuse interface simulations of
1082 contact line motion. Phys Rev E 75:046708 .
1083 https://doi.org/10.1103/PhysRevE.75.046708

1084 Ferrari A, Lunati I (2013) Direct numerical simulations of interface dynamics to link
1085 capillary pressure and total surface energy. Adv Water Resour 57:19–31 .
1086 https://doi.org/10.1016/j.advwatres.2013.03.005

1087 Frank F, Liu C, Alpak FO, Berg S, Riviere B (2018) Direct Numerical Simulation of
1088 Flow on Pore-Scale Images Using the Phase-Field Method. SPE J 23:1,833-
1089 1,850 . https://doi.org/10.2118/182607-PA

1090 Graveleau M, Soulaine C, Tchelepi HA (2017) Pore-Scale Simulation of Interphase
1091 Multicomponent Mass Transfer for Subsurface Flow. Transp Porous Media
1092 120:287–308 . https://doi.org/10.1007/s11242-017-0921-1

1093 Guido S, Villone M (1999) Measurement of Interfacial Tension by Drop Retraction
1094 Analysis. J Colloid Interface Sci 209:247–250 .
1095 https://doi.org/10.1006/jcis.1998.5818

1096 Haroun Y, Legendre D, Raynal L (2010) Volume of fluid method for interfacial
1097 reactive mass transfer: Application to stable liquid film. Chem Eng Sci
1098 65:2896–2909 . https://doi.org/10.1016/j.ces.2010.01.012

1099 Hasan S, Joekar-Niasar V, Karadimitriou NK, Sahimi M (2019) Saturation
1100 Dependence of Non-Fickian Transport in Porous Media. Water Resour Res
1101 55:1153–1166 . https://doi.org/10.1029/2018WR023554

1102 Hassanizadeh SM, Gray WG (1990) Mechanics and thermodynamics of multiphase
1103 flow in porous media including interphase boundaries. Adv Water Resour
1104 13:169–186 . https://doi.org/10.1016/0309-1708(90)90040-B

1105 Jacqmin D (1999) Calculation of Two-Phase Navier–Stokes Flows Using Phase-Field
1106 Modeling. J Comput Phys 155:96–127 .
1107 https://doi.org/10.1006/jcph.1999.6332

1108 Joekar-Niasar V, Hassanizadeh SM, Leijnse A (2008) Insights into the Relationships
1109 Among Capillary Pressure, Saturation, Interfacial Area and Relative
1110 Permeability Using Pore-Network Modeling. Transp Porous Media 74:201–
1111 219 . https://doi.org/10.1007/s11242-007-9191-7

1112 Kang Q, Lichtner PC, Viswanathan HS, Abdel-Fattah AI (2010) Pore Scale Modeling
1113 of Reactive Transport Involved in Geologic CO2 Sequestration. Transp Porous
1114 Media 82:197–213 . https://doi.org/10.1007/s11242-009-9443-9

1115 Kang Q, Lichtner PC, Zhang D (2006a) Lattice Boltzmann pore-scale model for
1116 multicomponent reactive transport in porous media: MULTICOMPONENT
1117 REACTIVE TRANSPORT. J Geophys Res Solid Earth 111:n/a-n/a .
1118 https://doi.org/10.1029/2005JB003951

1119 Kang Q, Lichtner PC, Zhang D (2006b) Lattice Boltzmann pore-scale model for
1120 multicomponent reactive transport in porous media. J Geophys Res Solid
1121 Earth 111: . https://doi.org/10.1029/2005JB003951

1122 Karadimitriou NK, Joekar-Niasar V, Babaei M, Shore CA (2016) Critical Role of the
1123 Immobile Zone in Non-Fickian Two-Phase Transport: A New Paradigm.
1124 Environ Sci Technol 50:4384–4392 . https://doi.org/10.1021/acs.est.5b05947

1125 Karadimitriou NK, Joekar-Niasar V, Brizuela OG (2017) Hydro-dynamic Solute
1126 Transport under Two-Phase Flow Conditions. Sci Rep 7:1–7 .
1127 https://doi.org/10.1038/s41598-017-06748-1

1128 Keller AA, Blunt MJ, Roberts APV (1997) Micromodel Observation of the Role of
1129 Oil Layers in Three-Phase Flow. Transp Porous Media 26:277–297 .
1130 https://doi.org/10.1023/A:1006589611884

1131 Khan AU-H, Jury WA (1990) A laboratory study of the dispersion scale effect in
1132 column outflow experiments. J Contam Hydrol 5:119–131 .
1133 https://doi.org/10.1016/0169-7722(90)90001-W

1134 Liu H, Valocchi AJ, Werth C, Kang Q, Oostrom M (2014) Pore-scale simulation of
1135 liquid CO2 displacement of water using a two-phase lattice Boltzmann model.
1136 Adv Water Resour 73:144–158 .
1137 https://doi.org/10.1016/j.advwatres.2014.07.010

1138 Liu H, Zhang Y, Valocchi AJ (2015) Lattice Boltzmann simulation of immiscible
1139 fluid displacement in porous media: Homogeneous versus heterogeneous pore
1140 network. Phys Fluids 27:052103 . https://doi.org/10.1063/1.4921611

1141 Maes J, Soulaine C (2018) A new compressive scheme to simulate species transfer
1142 across fluid interfaces using the Volume-Of-Fluid method. Chem Eng Sci
1143 190:405–418 . https://doi.org/10.1016/j.ces.2018.06.026

1144 McDonald K, Carroll KC, Brusseau ML (2016a) Comparison of Fluid-Fluid
1145 Interfacial Areas Measured with X-ray Microtomography and Interfacial
1146 Partitioning Tracer Tests for the same Samples. Water Resour Res 52:5393–
1147 5399 . https://doi.org/10.1002/2016WR018775

1148 McDonald K, Carroll KC, Brusseau ML (2016b) Comparison of fluid-fluid interfacial
1149 areas measured with X-ray microtomography and interfacial partitioning tracer
1150 tests for the same samples. Water Resour Res 52:5393–5399 .
1151 https://doi.org/10.1002/2016WR018775

1152 Meakin P, Tartakovsky AM (2009) Modeling and simulation of pore-scale multiphase
1153 fluid flow and reactive transport in fractured and porous media. Rev Geophys
1154 47: . https://doi.org/10.1029/2008RG000263

1155 Miller CT, Poirier-McNeil MM, Mayer AS (1990) Dissolution of Trapped
1156 Nonaqueous Phase Liquids: Mass Transfer Characteristics. Water Resour Res
1157 26:2783–2796 . https://doi.org/10.1029/WR026i011p02783

1158 Montemagno CD, Gray WG (1995) Photoluminescent volumetric imaging: A
1159 technique for the exploration of multiphase flow and transport in porous
1160 media. Geophys Res Lett 22:425–428 . https://doi.org/10.1029/94GL02697

1161 Peche A, Halisch M, Bogdan Tatomir A, Sauter M (2016) Development of a
1162 numerical workflow based on µ-CT imaging for the determination of capillary
1163 pressure–saturation-specific interfacial area relationship in 2-phase flow pore-
1164 scale porous-media systems: a case study on Heletz sandstone. Solid Earth
1165 7:727–739 . https://doi.org/10.5194/se-7-727-2016

1166 Porter ML, Wildenschild D, Grant G, Gerhard JI (2010) Measurement and prediction
1167 of the relationship between capillary pressure, saturation, and interfacial area
1168 in a NAPL-water-glass bead system. Water Resour Res 46: .
1169 https://doi.org/10.1029/2009WR007786

1170 Rallison JM (1984) The Deformation of Small Viscous Drops and Bubbles in Shear
1171 Flows. Annu Rev Fluid Mech 16:45–66 .
1172 https://doi.org/10.1146/annurev.fl.16.010184.000401

1173 Raoof A, Nick HM, Hassanizadeh SM, Spiers CJ (2013) PoreFlow: A complex pore-
1174 network model for simulation of reactive transport in variably saturated porous
1175 media. Comput Geosci 61:160–174 .
1176 https://doi.org/10.1016/j.cageo.2013.08.005

1177 Reeves PC, Celia MA (1996) A Functional Relationship Between Capillary Pressure,
1178 Saturation, and Interfacial Area as Revealed by a Pore-Scale Network Model.
1179 Water Resour Res 32:2345 . https://doi.org/10.1029/96WR01105

1180 Rokhforouz MR, Akhlaghi Amiri HA (2017) Phase-field simulation of counter-
1181 current spontaneous imbibition in a fractured heterogeneous porous medium.
1182 Phys Fluids 29:062104 . https://doi.org/10.1063/1.4985290

1183 Rokhforouz MR, Akhlaghi Amiri HA (2018) Pore-level influence of micro-fracture
1184 parameters on visco-capillary behavior of two-phase displacements in porous
1185 media. Adv Water Resour 113:260–271 .
1186 https://doi.org/10.1016/j.advwatres.2018.01.030

1187 Rokhforouz MR, Akhlaghi Amiri HA (2019) Effects of grain size and shape
1188 distribution on pore-scale numerical simulation of two-phase flow in a
1189 heterogeneous porous medium. Adv Water Resour 124:84–95 .
1190 https://doi.org/10.1016/j.advwatres.2018.12.008

1191 Schaffer M, Maier F, Licha T, Sauter M (2013) A new generation of tracers for the
1192 characterization of interfacial areas during supercritical carbon dioxide

injections into deep saline aquifers: Kinetic interface-sensitive tracers (KIS tracer). Int J Greenh Gas Control 14:200–208 . https://doi.org/10.1016/j.ijggc.2013.01.020

Smedt FD, Wierenga PJ (1984) Solute Transfer Through Columns of Glass Beads. Water Resour Res 20:225–232 . https://doi.org/10.1029/WR020i002p00225

Sun DL, Tao WQ (2010) A coupled volume-of-fluid and level set (VOSET) method for computing incompressible two-phase flows. Int J Heat Mass Transf 53:645–655 . https://doi.org/10.1016/j.ijheatmasstransfer.2009.10.030

Sussman M, Puckett EG (2000) A Coupled Level Set and Volume-of-Fluid Method for Computing 3D and Axisymmetric Incompressible Two-Phase Flows. J Comput Phys 162:301–337 . https://doi.org/10.1006/jcph.2000.6537

Tatomir A, Gao H, Pötzl C, Karadimitriou NK, Licha T, Class H, Helmig R, Sauter M (2020) Estimation of NAPL-Water interfacial areas for unconsolidated porous media by kinetic interface sensitive (KIS) tracers (submitted). Water Resour Res

Tatomir A, Vriendt KD, Zhou D, Gao H, Duschl F, Sun F, Licha T, Sauter M (2018) Kinetic Interface Sensitive Tracers: Experimental Validation in a Two-Phase Flow Column Experiment. A Proof of Concept. Water Resour Res 54:10,223-10,241 . https://doi.org/10.1029/2018WR022621

Tatomir A, Zhou D, Gao H, Dimache A-N, Iancu I, Sauter M (2019) Modelling of kinetic interface sensitive tracers reactive transport in 2D two-phase flow heterogeneous porous media. E3S Web Conf 85:07003 . https://doi.org/10.1051/e3sconf/20198507003

Tatomir AB, Halisch M, Duschl F, Peche A, Wiegand B, Schaffer M, Licha T, Niemi A, Bensabat J, Sauter M (2016a) An integrated core-based analysis for the characterization of flow, transport and mineralogical parameters of the Heletz pilot CO2 storage site reservoir. Int J Greenh Gas Control 48, Part 1:24–43 . https://doi.org/10.1016/j.ijggc.2016.01.030

Tatomir AB, Jyoti A, Sauter M (2016b) Monitoring of CO2 Plume Migration in Deep Saline Formations with Kinetic Interface Sensitive Tracers (A Numerical Modelling Study for the Laboratory). In: Vishal V, Singh TN (eds) Geologic Carbon Sequestration: Understanding Reservoir Behavior. Springer International Publishing, Cham, pp 59–80

Tatomir AB, Schaffer M, Kissinger A, Hommel J, Nuske P, Licha T, Helmig R, Sauter M (2015) Novel approach for modeling kinetic interface-sensitive (KIS) tracers with respect to time-dependent interfacial area change for the optimization of supercritical carbon dioxide injection into deep saline aquifers. Int J Greenh Gas Control 33:145–153 . https://doi.org/10.1016/j.ijggc.2014.11.020

van Genuchten MT, Wierenga PJ (1976) Mass Transfer Studies in Sorbing Porous Media I. Analytical Solutions 1. Soil Sci Soc Am J 40:473–480 . https://doi.org/10.2136/sssaj1976.03615995004000040011x

Wildenschild D, Sheppard AP (2013) X-ray imaging and analysis techniques for quantifying pore-scale structure and processes in subsurface porous medium systems. Adv Water Resour 51:217–246 . https://doi.org/10.1016/j.advwatres.2012.07.018

Yang L, Nieves-Remacha MJ, Jensen KF (2017) Simulations and analysis of multiphase transport and reaction in segmented flow microreactors. Chem Eng Sci 169:106–116 . https://doi.org/10.1016/j.ces.2016.12.003

Yin X, Zarikos I, Karadimitriou NK, Raoof A, Hassanizadeh SM (2019) Direct simulations of two-phase flow experiments of different geometry complexities using Volume-of-Fluid (VOF) method. Chem Eng Sci 195:820–827 . https://doi.org/10.1016/j.ces.2018.10.029

Yiotis AG, Psihogios J, Kainourgiakis ME, Papaioannou A, Stubos AK (2007) A lattice Boltzmann study of viscous coupling effects in immiscible two-phase flow in porous media. Colloids Surf Physicochem Eng Asp 300:35–49 . https://doi.org/10.1016/j.colsurfa.2006.12.045

Yue P, Feng JJ, Liu C, Shen J (2004) A diffuse-interface method for simulating two-phase flows of complex fluids. J Fluid Mech 515:293–317 . https://doi.org/10.1017/S0022112004000370

Yue P, Zhou C, Feng JJ, Ollivier-Gooch CF, Hu HH (2006) Phase-field simulations of interfacial dynamics in viscoelastic fluids using finite elements with adaptive meshing. J Comput Phys 219:47–67 . https://doi.org/10.1016/j.jcp.2006.03.016